

¹ **Floating wind farm experiments through scaling for wake
2 characterization, power extraction and turbine dynamics**

³ Juliaan Bossuyt ¹, Ondřej Ferčák ¹, Zein Sadek¹, Charles
⁴ Meneveau², Dennice F. Gayme², and Raúl Bayoán Cal¹

⁵ *Department of Mechanical and Materials Engineering,
6 Portland State University, Portland, Oregon, USA and*

⁷ *2 Department of Mechanical Engineering,
8 Johns Hopkins University, Baltimore, MD 21218, USA*

Abstract

In this study, wind and water tunnel experiments of turbulent wakes in a scaled floating wind farm are performed. Scaling of a floating wind farm with a scaling ratio of 1:400 is made possible by relaxing geometric scaling of the turbine platform system, such that the dynamic response can be correctly matched, and to allow for relaxing Froude scaling such that the Reynolds number can be kept large enough. Four dimensionless parameters, describing the relative importance of wind and wave loads compared to turbine inertia, are used to guide the scaled floater design. Free decay tests of the pitch and heave response confirm that the dimensionless natural frequency of the scaled model is in the typical range for full-scale floating turbines when matching the proposed four dimensionless parameters.

The response and performance of a single turbine scaled model are characterised for different wind and wave conditions. Subsequently, a wind farm experiment is performed with twelve floating turbine models, organised in four rows and three columns. Particle image velocimetry measurements of the wake of the middle turbine in the third row reveal distinct differences in wake properties for different wave conditions. Conditional averaging confirms a synchronization of wake deflection with the traveling waves in the wind farm. The power outputs show distinct peaks at the wave frequencies and its harmonics, due to motions triggered by complex wave-turbine-wake interactions. The power spectrum of the aggregate power of three streamwise aligned turbines exhibits anti-correlation of motions at the wave frequency due to wave-speed-induced phase-lag, and spatio-temporal correlations of power outputs at the frequency corresponding to the wind-convective time between two rows. These experiments using an appropriately scaled floating wind farm in a wind tunnel setup confirm distinct impacts of turbine motion on wake recovery and meandering, and measurement results highlight the intricate interactions between wave topology, and wake meandering.

I. INTRODUCTION

The vast wind-energy potential above deep ocean waters has motivated increasing government investment in the development of floating wind plants. At the end of 2022, 15GW of floating wind capacity was auctioned on the US west-coast, to be installed by 2035 [1]. A total of 23GW floating wind capacity is planned in Scottish waters, of which 18GW was

¹⁴ auctioned in 2022 [2], and Portugal increased its goal for floating wind energy with an aim
¹⁵ to auction 10GW of capacity in 2023 [3]. The world's first commercial floating wind farm,
¹⁶ the 30MW Hywind in Scotland, has hit record high power-capacity factors [2]. Estimates
¹⁷ show that there is significant potential to reduce costs as indicated by the U.S. Department
¹⁸ of Energy's plans to reduce costs of floating wind by 70% by 2035 [4]. However, a better
¹⁹ understanding of the complex interactions between different types of ocean waves and tur-
²⁰ bulent winds is needed to further improve turbine and platform designs and robustness, as
²¹ well as to reduce the cost of floating wind energy. The associated improvements to system
²² reliability and lower costs are imperative for floating wind to play a significant role in helping
²³ to respond to the global demands to transition to renewable energy sources.

²⁴ Platform stability and unsteady loading are two main topics early studies have focused
²⁵ on to enable floating wind technology [5–8]. Advanced water basin tests, with Froude scaled
²⁶ floating wind turbines have allowed for accurate quantification of dynamic response to in-
²⁷ coming wave and wind conditions [5]. The results have been essential for the validation
²⁸ of numerical simulations of floating wind turbine dynamics. Froude scaling is required for
²⁹ scaled experiments to simulate the hydrodynamic response to the incoming wave field cor-
³⁰ rectly [9]. Froude scaling focuses on the ratio of flow momentum to gravitational forces, and
³¹ is a proven approach for scaling hydrodynamic experiments. However, Reynolds number
³² scaling requires higher wind speeds than Froude scaling and is therefore very difficult to
³³ be satisfied simultaneously. As a result, Froude scaled tests are challenged in reproducing
³⁴ realistic thrust and power coefficients [10]. The topic of several studies has, therefore, been
³⁵ to develop solutions to simulate wind forces, for example, by using low-Reynolds number
³⁶ rotors, porous disks, ducted fans, or propellers to generate representative thrust [10]. The
³⁷ Reynolds number is an important limitation of Froude-scaled tests, typically limiting the
³⁸ scaling ratios to be on the order of 1:50. As a result, Froude scaled models typically have a
³⁹ rotor diameter on the order of 2m or larger. Due to these large rotor diameters, combined
⁴⁰ with challenges in generating realistic aerodynamic performances, Froude scaled tests make
⁴¹ it very challenging to study the impact of turbine motion on wake characteristics especially
⁴² in typical wind tunnel facilities for which test sections much larger than 2m would be re-
⁴³ quired (i.e. to produce precisely controlled wind conditions and measurements, as opposed
⁴⁴ to open water basin tests with external fans).

⁴⁵ To overcome these challenges, research has focused on wake properties of static misaligned

⁴⁶ rotors [11–18] and rotors subject to oscillating motions, such as pitch, heave, and surge [19–
⁴⁷ 26], without considering the hydrodynamic two-way coupling with wave motions. Messmer
⁴⁸ et al. [25] provides a recent overview and discussion of wake behavior for moving rotors.
⁴⁹ By prescribing actuated rotor motions, experiments can ensure aerodynamic scaling of wake
⁵⁰ properties more easily. Simulations [19, 27–35] and experimental studies [20, 36–45] have
⁵¹ shown a strong sensitivity of wake properties to the dynamic motion of a wind turbine
⁵² rotor. Depending on the dimensionless frequency of the rotor motion, or Strouhal number
⁵³ ($S_t = fD/U_h$, with f being the frequency of motion, D the rotor diameter, and U_h the inflow
⁵⁴ wind speed at hub height), wake recovery can be accelerated. Especially for higher Strouhal
⁵⁵ numbers, an amplification of the wake meandering amplitude has been observed, leading
⁵⁶ to non-linear wake dynamics and faster wake recovery [25]. A differentiation can be made
⁵⁷ between slow rotor motions (e.g. $St < 0.05$) leading to wake deflection and displacement,
⁵⁸ and faster motions (e.g. $St > 0.2$) [25, 40], leading to this amplification of wake meandering
⁵⁹ amplitude and non-linear wake dynamics. Both operating zones need to be studied, given
⁶⁰ the large range of time scales describing the motion of a floating wind turbine.

⁶¹ Due to wake spreading, turbine power in the fully developed region of large wind farms
⁶² becomes governed by vertical transport of mean kinetic energy from the high momentum
⁶³ flow above [46–58]. Therefore, it is important to study the impact of floating turbine motions
⁶⁴ on wake recovery in a wind farm setting, where turbines are subject to wake turbulence from
⁶⁵ many upstream turbines. Yang et al. [59] performed Large Eddy Simulations (LES) of a fixed
⁶⁶ bottom offshore wind farm exposed to large period ocean waves, as well as shorter-period
⁶⁷ localized wind-driven waves. Those LES results indicate the importance of considering the
⁶⁸ wave-wind-turbine coupling in studying the wake characteristics and available power. More
⁶⁹ specifically, it was found that large period swell waves can increase the downwards transfer
⁷⁰ of mean kinetic energy in a fully developed wind farm array. More recently, Ferčák et al.
⁷¹ [60] performed wind tunnel tests of a fixed bottom wind turbine subject to long period swell
⁷² waves. In that work wave topology was also found to impact the wake recovery and velocity
⁷³ profile to heights as high as the turbine tip height. An LES study by Yang et al. [61] showed
⁷⁴ that lateral swell waves can cause wake deflection, due to the locally induced change in wind
⁷⁵ direction.

⁷⁶ It is evident that floating turbine wakes can be influenced by wave conditions and rotor
⁷⁷ motions, thus leading to a complex turbine-wind-wave coupling. In a floating wind farm, this

78 interaction can extend over groups of turbines as the turbine/platform motion and wakes
79 affect each other. Such couplings can lead to not only improved (or reduced) power output,
80 but also to power fluctuations at dominant frequencies related to the farm layout, the wind,
81 and wave conditions. There is a need for experimental data of such wind-wave-wake-turbine
82 interactions in a floating wind farm, for validation and to study in more detail the underlying
83 mechanisms. However, due to the practical testing limitations described above, most wind
84 tunnel studies of floating wind turbine wakes have focused on prescribing the rotor motion
85 while using a fixed wind tunnel floor (i.e. without a free surface and waves), thus ignoring
86 dynamic wave-turbine interactions.

87 Here, a scaling methodology for floating wind farm experiments using laboratory wind
88 and water tunnel setups is presented. The proposed scaling method strikes a balance be-
89 tween the desirability of matching different dimensionless groups (Reynolds number, Froude
90 number, Strouhal numbers, thrust coefficient, tip speed ratio, etc.), and practical restric-
91 tions which inevitably mean that not all of these groups can be matched simultaneously
92 for the large scale ratios required (typically 1:200 to 1:1000 and above). In analogy with
93 the use of low-Reynolds number airfoil profiles (i.e. a change of rotor geometry) for scaled
94 turbine models that enables to relax the matching of the Reynolds numbers, an approach in
95 which floater geometry designs are changed to reproduce the correct dynamic response and
96 enable to relax matching the Froude numbers is proposed. Floaters are designed in a man-
97 ner that improves the turbine/platform hydrodynamic response. Specifically, a small-scale
98 floating wind turbine model that is designed to approximate full scale turbine motions, as
99 characterized by appropriately redefined Strouhal numbers and scaled motion-amplitudes, is
100 introduced. Based on typical offshore weather, and the dominant factors determining float-
101 ing turbine motion, conditions with long-period swell waves and high wind speed are selected.
102 By combining turbine power, turbine motion, wave motion and wake measurements, the aim
103 is to reproduce the dominant features of wind loads, wave fields, and platform motion, their
104 interactions and effects on wake behavior and wind farm performance.

105 Following a discussion of the scaling methodology in section II, the measurement tech-
106 niques are documented in section III. In section IV the experimental setup, the scaled
107 floating turbine, wind farm, and wave conditions are presented. Section V presents the
108 measured performance of a single floating turbine. In the final section VI, the wake, motion
109 and power measurements of the scaled floating wind farm are presented and discussed.



FIG. 1. Photograph of the scaled floating wind farm setup in the Portland State University wind- and water tunnel.

¹¹⁰ **II. SCALING METHODOLOGY**

¹¹¹ Offshore wind turbines have a diameter that typically ranges from about 60m to 120m,
¹¹² becoming increasingly larger with new developments. Conversely, a scaled turbine model for
¹¹³ wind farm experiments in a typical wind tunnel, requires rotor diameters on the order of 0.1-
¹¹⁴ 0.3m [13, 62–64]. The corresponding required geometrical scaling ratios are thus typically
¹¹⁵ between 1:200 to 1:1200, making the scaling very challenging.

¹¹⁶ One of the main challenges for performing scaled experiments of floating bodies is scaling
¹¹⁷ the aerodynamic and hydrodynamic (interactions with the free surface) conditions simul-
¹¹⁸ taneously, one requiring similarity of Reynolds number ($Re_D = U_h D / \nu$), tip speed ratio
¹¹⁹ ($TSR = \omega R / U_h$), thrust coefficient ($C_T = 2F_{WT} / \rho U_h^2 A$), power coefficient ($C_p = 2P / \rho U_h^3 A$),
¹²⁰ and Strouhal number of rotor motions ($S_t = f D / U_h$), while the other mainly requiring
¹²¹ Froude Number scaling ($Fr = U_h / \sqrt{gD}$). In these equations, U_h is the incoming mean wind
¹²² speed at hub height, D the turbine diameter, ν the kinematic viscosity of air, ω the angular
¹²³ speed of the rotor, A the cross-sectional area of the rotor, ρ the density of the fluid, f the
¹²⁴ frequency of the motion, and g the gravitational acceleration.

¹²⁵ The Froude number is relevant for flows in which the inertial forces occur together with
¹²⁶ gravitational forces, and thus for free surface flows in general [65]. Froude number scaling
¹²⁷ can also become important for matching the relative inertia of an object when studying
¹²⁸ the interaction with wind loading and the resulting dynamic motion. This requirement is
¹²⁹ discussed specifically for a floating turbine below.

If the same medium is used for scaled tests, air and water in this case, only one dynamic scaling ratio can be fulfilled simultaneously [66]. For example, given a typical rotor mass on the order of 100,000kg or more, and a rated wind speed of 12m/s for a 5MW wind turbine [67], a Froude scaled turbine with a scaling ratio of 1 : 600 should have a rotor mass of 0.0005 kg, and would have to be tested with a wind tunnel speed of 0.5m/s. It is not possible to build a working 0.5 gram model turbine and the Reynolds number would be too small to reproduce realistic wake properties.

Therefore, in typical scaled tests of coastal processes length-scale ratios are typically limited to about 1 : 50 [68], and Reynolds similarity is almost always relaxed, as gravitational forces are predominant in free-surface flows [65].

For floating wind turbine applications, the effects of Reynolds number have to be taken into account, even if perfect similarity (matching Reynolds numbers) cannot be enforced. Given this, it is not possible to match Reynolds numbers with a model turbine [69] (using the same fluid at standard atmospheric conditions, a length-scale ratio of 600 would imply that one needs to run the wind tunnel at speeds 600 times that of wind, i.e. hypersonic speeds). If the same rotor geometry would be used in scaled wind tunnel tests at lower Reynolds numbers, the reduced lift generated by the blades due to the much lower Reynolds number would result in an unrealistically small power coefficient, thrust coefficient and tip speed ratio [62, 70, 71]. To circumvent this challenge, experimental wind tunnel studies use airfoil profiles more suitable for low Reynolds numbers, and with larger chord lengths to reproduce realistic full-scale lift coefficient, as visualised in figure 2 (b). This approach is well established [13, 60, 62, 64, 72, 73] for wind tunnel testing of wind farms, and though the Reynolds number is not matched, the main properties of turbine wakes in turbulent boundary layers can be captured as long as the model Reynolds number is held above a critical Reynolds number, $Re_D > 2 - 4.8 \times 10^4$ [63, 72, 74]. This is an example of a scaling approach in which geometric similarity is relaxed (e.g. blade profile), in order to better match the essential dimensionless parameters for wake properties (thrust coefficient, power coefficient, and tip speed ratio).

Similarly, for scaled tests of a floating wind turbine with a scaling ratio in the range of 1:200 to 1:1000, exact Froude scaling is impossible even if the Reynolds number is not matched and is only kept high enough above the critical value needed ($Re_D > Re_{D,crit}$) as described before. As a result of not following Froude number scaling, the scaled model will

162 have a relatively larger inertia compared to the external loads, thus affecting its response to
 163 wind and wave loads. Therefore, the approach followed in this paper considers a redesign of
 164 the floating structure to match the important dimensionless numbers for wake properties;
 165 the Strouhal number and dimensionless measures of the amplitude of the six degrees of
 166 freedom (i.e. sway, heave, surge, pitch, yaw, and roll as indicated in figure 2).

167 In practice, the motions of a floating turbine are strongly determined by its natural fre-
 168 quencies [5, 75]. Therefore, the dimensionless natural frequencies (i.e. as a Strouhal number)
 169 need to be matched as closely as possible. A floating turbine can be approximated by a har-
 170 monic oscillator with external loading (e.g. wind, waves, and elastic mooring forces). To
 171 match the natural frequency for a scaled model that is relatively heavier due to not matching
 172 Froude scaling, the hydraulic restoring force and moment can be altered by changing the
 173 floater design.

174 The motion of a floating turbine is described by the balance of all forces \vec{F}_i and moments
 175 \vec{M}_i in each direction (Newton's second law for translation and rotation), as:

$$\sum \vec{F}_i = m \vec{a}, \quad (1)$$

176 and

$$\sum \vec{M}_i = \mathbf{I} \vec{\alpha}, \quad (2)$$

177 leading to one equation for each motion (sway, heave, surge, roll, pitch and yaw). Here, m is
 178 the mass of the entire turbine, \vec{a} the acceleration, \mathbf{I} the rotational mass-moment of inertia,
 179 and $\vec{\alpha}$ the angular acceleration, implicitly including the effects of added mass, hydrostatic
 180 forces, damping, and external forces. Figure 2 (a) presents a schematic representation of
 181 different forces acting on a real floating wind turbine. For a floating wind turbine the wind
 182 force is mainly balanced by inertia of the turbine and structure, floater-drag-loads, buoyancy
 183 forces generated by the floaters, and mooring forces. The floater-drag-loads have a compo-
 184 nent due to frictional losses and form-drag losses. (Reproducing the full-scale conditions,
 185 water surface-tension effects need to be negligible in the model as well). To scale the motion
 186 of a floating turbine, it is thus important that the relative contribution of each term in
 187 equation 1 and 2 is similar. Therefore, several ratios of forces and moments are considered
 188 next, in order to scale the relative impact of wind and wave loads on the motion of a floating
 189 turbine. Four main dimensionless ratios of interest are selected for this study.

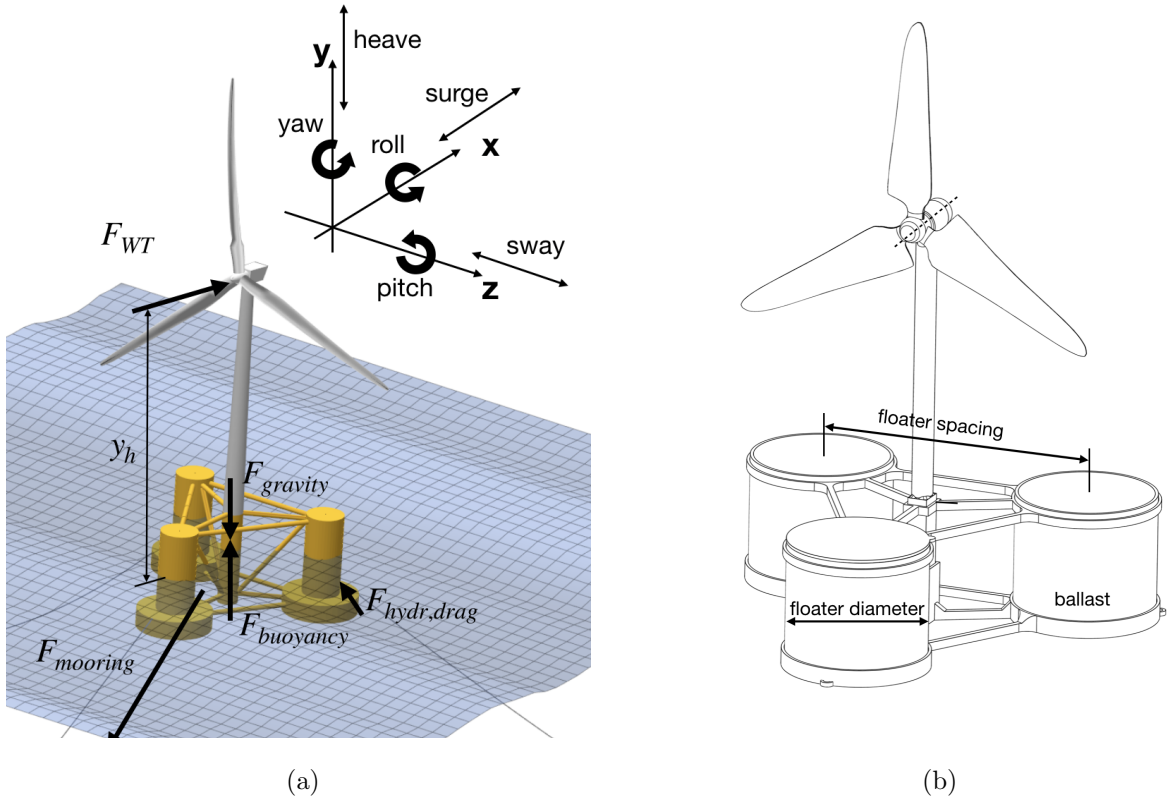


FIG. 2. A schematic representation of several forces acting on a floating turbine, represented on the OC5 DeepCWind turbine with NREL 5MW rotor as visualised in QBlade [76] (a), and a schematic representation of floater design parameters that can be altered to improve the response of a small-scale model (b).

190 The relevant scale for acceleration is chosen as $a_0 = U_h^2/D$, with U_h the incoming hub
 191 wind speed, and D the rotor diameter. The scale for angular acceleration is chosen as: $\alpha_0 =$
 192 $\Delta\theta U_h^2/D^2$, with $\Delta\theta = 1\text{deg}$ chosen arbitrarily, but not affecting the comparison between
 193 full-scale and scaled model given the objective of similar angular displacement for kinematic
 194 similarity.

195 The ratio of wind-thrust-force F_{WT} to turbine inertia ma_0 represents the sensitivity of
 196 surge turbine acceleration to wind load fluctuations:

$$R1 = \frac{F_{WT}}{ma_0} \quad (3)$$

197 with:

$$F_{WT} \sim \frac{1}{2} \rho_{air} U_h^2 A C_T, \quad (4)$$

and ρ_{air} the density of air, and A the rotor area. Using the relation for wind thrust and acceleration scale, the ratio reduces to $R1 \sim 1/8\rho_{air}\pi D^3 C_T/m$. Keeping this ratio constant for a scaled model, and given that we do not want to change C_T to preserve correct wake properties, the mass needs to scale with D^3 , which is the same requirement as for Froude scaling [77].

The ratio of heave response force $\Delta F_{hydr,\Delta h}$ to turbine inertia ma_0 , characterizes the responsiveness of the floating structure to incoming waves or heave motions in general. Considering the geometric scaling of wave conditions and wind turbine size, the ratio is calculated for submerging the turbine with a fixed depth scaled by turbine diameter $\Delta h = D$. The ratio is written as:

$$R2 = \frac{\Delta F_{hydr,\Delta h}}{ma_0}, \quad (5)$$

with

$$\Delta F_{hydr,\Delta h} \sim \rho_{water} A_{platform} D g. \quad (6)$$

In this equation, ρ_{water} is the density of water, and $A_{platform}$ the total floater cross-sectional area at the water surface. Thus, $R2 = (\rho_{water} A_{platform} D^2 g) / (m U_h^2)$, giving a relation for the cross-sectional area of the floating platform as a function of the geometric scaling, the ratio of wind speeds, and the ratio of mass. If the analogy is made with a harmonic oscillator description of a floating turbine, this ratio of a spring force to turbine mass reflects the scaling of the squared dimensionless natural frequency to heave motions. By manipulating the cross-sectional area of the model, the aim is to match R2 between full scale and model conditions as well as possible.

For pitching motions, the moment generated by the wind-thrust force M_{WT} is compared to the rotational inertia of the floating turbine for pitch $I_z \alpha_0$. This ratio represents the sensitivity of the pitching motion of the turbine to wind velocity fluctuations:

$$R3 = \frac{M_{WT}}{I_z \alpha_0}, \quad (7)$$

with

$$M_{WT} \sim y_h F_{WT}, \quad (8)$$

resulting in

$$R3 = \frac{1}{2} \frac{\rho \pi C_T}{\Delta \theta} \frac{D^5}{I_z}. \quad (9)$$

222 It is also desireable to match R3 as closely as possible. Similarly as for ratio R1, since the
 223 wind speed and turbine diameter are used as a scaling for time, velocity and acceleration, the
 224 only way to match R3 is by scaling the mass-moment of inertia with D^5 (unless a reduction
 225 in $\Delta\theta$ is acceptable), which corresponds to the same requirement as for Froude scaling [77].
 226 Technically, there is an opportunity to change the design such that the mass-moment of
 227 inertia scales with D^5 , though this would counteract the requirements for ratio R2 and R4.
 228 Inevitably, the rotational inertia of the scaled turbine to wind fluctuations will be relatively
 229 higher, so that only the large-scale velocity fluctuations will have an effect on pitch angle.
 230 Contrary to R1, the moment generated by the wind loads can be significant compared to
 231 rotational inertia for a full scale floating turbine (e.g. $R3 \approx 0.5$ as estimated for the OC5
 232 DeepCWind floating wind turbine design [75]). However, this ratio does not fully describe
 233 the turbine response to wind fluctuations, as other loads also play a role (e.g. the hydraulic
 234 floater-restoring-moment, the rotor gyroscopic inertia, among others). It is important to
 235 note that ratio R3 does not relate to the magnitude of pitch motions due to steady wind
 236 loads, but instead to the relative inertia of the turbine (i.e. the inertia of the turbine acts
 237 as a low pass filter to wind load fluctuations, such that the motion will mostly be governed
 238 by the large scale changes in wind loads).

239 The ratio of the hydraulic pitch restoring moment $M_{\Delta\theta}$ to the rotational inertia $I_z\alpha_0$
 240 indicates the responsiveness of the floating wind turbine to incoming waves. A higher ratio
 241 will correspond to a higher natural frequency for pitching. The ratio is written as:

$$R4 = \frac{M_{\Delta\theta}}{I_z\alpha_0}. \quad (10)$$

242 The R4 ratio needs to be calculated for a specific change in pitch angle, which is arbitrarily
 243 chosen as $\Delta\theta = 1\text{deg}$, as it will not impact the comparison between full-scale and model
 244 scale. For a semi-submersible design, one can aim to match this ratio by changing the
 245 diameter and spacing of the floaters.

246 III. MEASUREMENT TECHNIQUES

247 This section details the used measurement techniques. Particle Image Velocimetry (PIV)
 248 is used for wake measurements, Light Induced Fluorescence is used to measure the water
 249 height and wave properties, and a stereo-camera setup is used to optically track the motion

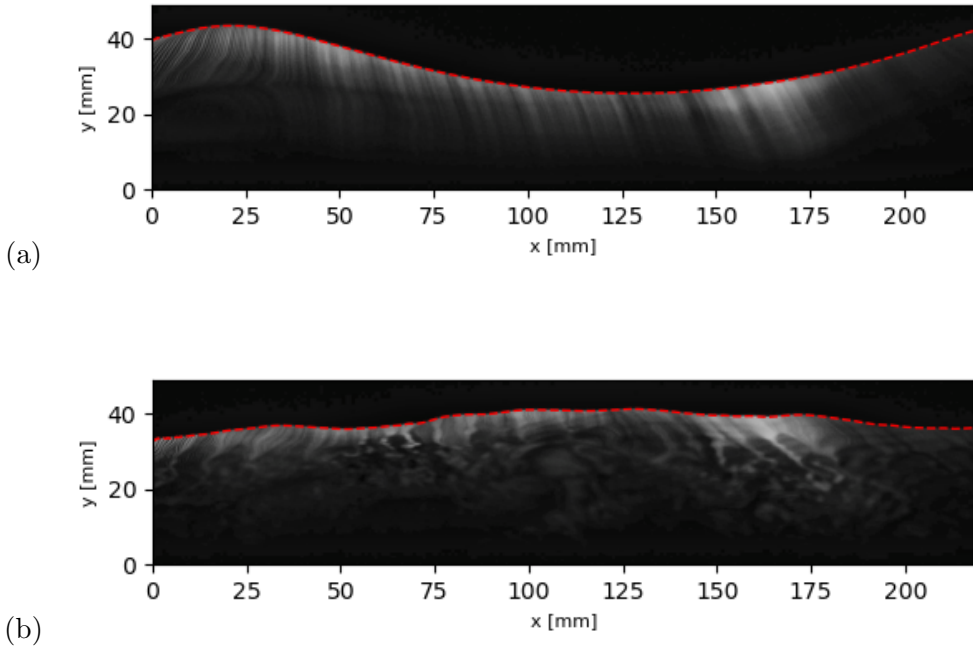


FIG. 3. Example of images used for water surface measurements. Standard computer vision algorithms are used to identify the air-water interface, as indicated by the red-dashed line. Figure (a) is for a wave frequency of 2.7Hz with no wind, while figure (b) is for a wave frequency of 1.5Hz and a wind speed of 5.4m/s.

250 of a floating turbine. The measurements make reference to an experimental setup (described
 251 in more detail later in §IV) in a closed-loop wind tunnel with a floor consisting of a water
 252 tank with wave paddle and wave-damper. Single or arrays of floating wind turbine models
 253 are placed on the water surface. A standard PIV measurement setup is used, which is
 254 detailed in Appendix A.

255 **A. Light Induced Fluorescence measurement of water interface**

256 The transient water-surface profile is measured using Light Induced Fluorescence (LIF)
 257 [78]. A setup with a FLIR BFS-U3-51S5M camera, a 532 nm optical filter, a 200 mW (532
 258 nm) continuous LED laser sheet, and a commercially available red fluorescent dye, is used to
 259 characterize the waves. A cropped region of interest is acquired using the camera sensor to
 260 cover only the region where the water height is visible, enabling a sampling rate increase to



FIG. 4. Camera snapshot used for optical tracking, with indication of tracked markers and their previous trajectory for an incoming hub wind speed of 2.9m/s and a 1.2Hz wave conditions.

261 250 Hz. Figure 3 shows an example of a recorded image for wave shape identification. Using
 262 standard image processing techniques, based on light intensity, the wave height is deduced
 263 from each image. The wave period is found from the frequency spectrum of wave height
 264 at a fixed location, and the wave-velocity from the time-lag corresponding to the maximum
 265 correlation between wave-height time signals at two points with maximum separation in the
 266 field of view. The uncertainty of the wave speed is estimated from the sampling frequency
 267 (± 0.01 s), distance between the two points, and the measured velocity itself. The wavelength
 268 λ and its uncertainty are derived from the measured wave period T and wave velocity V ,
 269 according to $\lambda = VT$. The estimated uncertainty on wave speed and wave length is $\pm 5\%$.
 270 See section IV B for more detail about the measured conditions.

271 **B. Optical Tracking of floating wind turbine**

272 The motion of the floating turbine is measured with a stereo-camera setup, using two
 273 FLIR BFS-U3-16S2C-CS cameras, with a 1.6MP resolution and a maximum frame rate of

²⁷⁴ 226 fps. Camera calibration and 3D reconstruction using line-of-sight is done following the
²⁷⁵ polynomial fitting approach by Machicoane et al. [79]. A calibration plate is accurately
²⁷⁶ positioned in increments of 10mm with a traversing system and captured by the camera
²⁷⁷ setup in the wind tunnel. Both cameras are synchronized with an external trigger signal at
²⁷⁸ a frequency of 200Hz, generated by an Arduino micro-controller. Each camera is connected
²⁷⁹ to a dedicated workstation to retrieve and save the frames. Checkerboard markers are
²⁸⁰ placed on the floating turbine and rotor, using decal paper. The markers are tracked using
²⁸¹ a combination of OpenCV tools in Python and a custom prediction step for the subsequent
²⁸² marker locations. The best accuracy of the marker positions is found using a cross-correlation
²⁸³ approach of the marker region with an ideal saddle-point pattern, and fitting a 2D polynomial
²⁸⁴ to the cross-correlation values to retrieve the location of the maximum value with sub-pixel
²⁸⁵ accuracy. Given that the angular position changes of the floating turbine are not large,
²⁸⁶ there is no need to include a rotational dependence for the saddle-point cross-correlation. A
²⁸⁷ series of high-power LED flood lights are used, powered by a DC power supply, to enable
²⁸⁸ a small exposure time for the cameras with global-shutter, as to freeze the motion of the
²⁸⁹ turbine blades. The error on reconstructing the calibration points is within $\pm 0.5\text{mm}$. On
²⁹⁰ one turbine, 13 chessboard-marker points are tracked on the tower, and one chessboard
²⁹¹ marker point on each floater. Knowing the relative positions of the marker points, from a
²⁹² calibration in standstill, the motion of the turbine is found from fitting the set of reference
²⁹³ marker locations to the measured locations using a minimization algorithm, giving the six
²⁹⁴ degrees of freedom: yaw, roll, pitch, heave, surge, and sway.

²⁹⁵ **IV. EXPERIMENTAL SETUP**

²⁹⁶ The closed-loop wind tunnel at Portland State University (PSU) has a test section with
²⁹⁷ a length 5 m, width 1.2m, and height 0.8m. A schematic representation of the wind tunnel
²⁹⁸ test section, with wave paddle, wave damper, and floating wind turbines is shown in figure
²⁹⁹ 5. The wind tunnel speed can range from 2 to 40 ms^{-1} , and the ceiling is configured to
³⁰⁰ approach a zero-pressure gradient boundary layer during the experiments. The sidewalls are
³⁰¹ assembled of Schlieren-grade annealed float glass fastened to the steel framework to ensure
³⁰² maximum optical access for the laser and camera [80–82]. An expansion-contraction section
³⁰³ with mesh in the low-speed zone reduces the background turbulence intensity at the inlet.

304 For the present experiments, no turbulence grid is used, resulting in a uniform low-turbulence
 305 inflow. The floor of the wind tunnel test-section is replaced by a water tank with wave paddle
 306 and wave-damper, as described in more detail in section IV B. A photograph of the scaled
 307 floating wind farm in the wind tunnel test section is shown in figure 1. In the following
 308 sections, the floating wind turbine model design, and wave conditions are described.

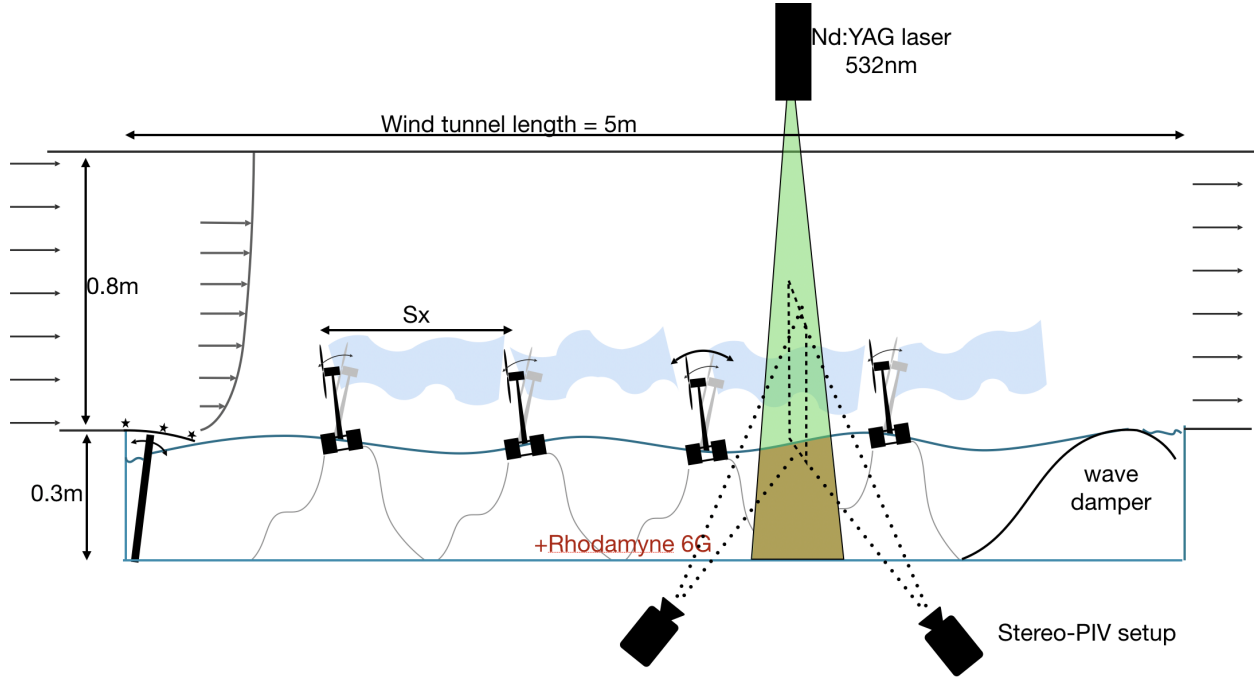


FIG. 5. Schematic representation of the measurement setup in the Portland State University wind tunnel

309 **A. Floating wind turbine**

310 The rotor design by Odemark and Fransson [83] is used and geometrically scaled from
 311 a diameter of $D = 0.226\text{m}$ to a diameter of $D = 0.15\text{m}$. The rotor is 3-D printed on a
 312 3D Systems ProJet MJP 3600 in high detail resin. The same rotor and size has already
 313 been used successfully in a previous wind tunnel study of a scaled fixed bottom offshore
 314 wind turbine [60]. A Faulhaber 1331T012SR direct current (DC) motor, with a diameter
 315 of 13mm is used as a DC generator to control the tip-speed-ratio. The maximum power
 316 coefficient is found for a tip speed ratio of $TSR = 5$ (see section V). The power coefficient
 317 is estimated to be $C_P \approx 0.25$, using the measured current and the motor torque constant

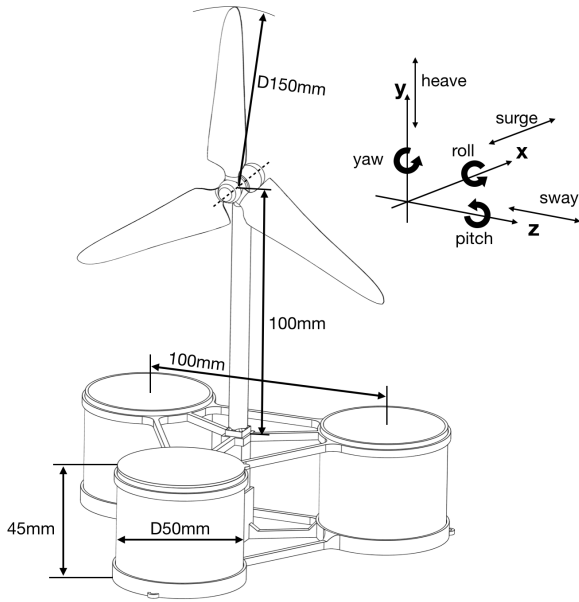


FIG. 6. Schematic of scaled down floating wind turbine model with key dimensions.

318 specified by the manufacturer, which gives a rough estimate following the discussion by
 319 Bastankhah and Porté-Agel [64]. The tip speed ratio (TSR) is controlled using a variable
 320 resistor to maximize the power coefficient. Thin 30 AWG silicone flexible electric wires are
 321 used to connect the DC generator of the floating turbine to a 200 Ohm variable resistor
 322 outside of the wind tunnel, as to minimize impact on motion due to wire stiffness. The rotor
 323 thrust coefficient is estimated to be $C_T \approx 0.65$ by measuring the turbine thrust force with a
 324 miniature double-beam load cell, and for the turbine in a fixed, non-floating position [60].
 325 As desired, the power coefficient is a good approximation of full-scale conditions (although
 326 still being somewhat smaller).

327 There are many different floater designs for floating wind turbines considered in the
 328 literature, and every design has its own characteristics and optimal use-cases. In this study
 329 the choice was made to scale a semi-submersible design, which has generally a stronger pitch
 330 response to incoming wave slope changes, and a motion which is more determined by the
 331 floater geometry instead of mainly the mooring stiffness. Furthermore, the semi-submersible
 332 DeepCWind design is well documented in the literature, and provides a useful reference for
 333 our experiments.

334 The most challenging part is matching the kinematic response of a full scale floating
 335 wind turbine, as determined mainly by the natural frequency (Strouhal number) of the

Rotor diameter	0.15m
Hub height above water line	0.113m
Total mass	164 gram
Mass rotor	4 gram
Mass DC generator	19 gram
Mass of tower + electric wires	16 gram
Mass of floater w/o ballast	56 gram
Mass of ballast	69 gram
Floater diameter	0.05m
Floater spacing	0.1m
Mass moment of inertia for pitch	$6.73 \times 10^{-4} \text{kgm}^2$

TABLE I. Geometric properties of the scaled down model.

turbine, and motion amplitudes. In this first scaling attempt, the objective is to design a model turbine matching the response of a full-scale floating turbine with a diameter of 60m, thus requiring a scaling ratio of 1:400. High wind speed conditions are considered, with a hub wind speed of 25m/s (close to its maximum limit). The floating platform of the OC5 DeepCwind turbine [75] is used as a reference for the 60m diameter rotor. Because the mass of the rotor and tower represents only 3% of the total mass, the OC5 DeepCwind floater properties (such as total mass, and mass moment of inertia) are not adjusted for the smaller rotor diameter, and the information documented by Robertson et al. [75] is used.

As discussed in section II, a minimum wind speed is required for the wind tunnel tests to have a sufficiently high Reynolds number for wake properties. To ensure a Reynolds number well above 20,000, we chose to operate the tunnel at a wind speed such that the hub wind speed inside the wind farm is around 2.9 m/s. Naturally at this small value, the Froude number cannot be matched with the full-scale system. To match Froude numbers, one would require a velocity ratio equal to $400^{1/2} = 20$, i.e. a wind tunnel speed less than 1 m/s which then implies a Reynolds number significantly below the desired threshold value of 20,000. A scaled model turbine is needed which can operate in higher wind speeds than required by strict Froude scaling (without capsizing), yet has a representative dynamic response to wind and wave loads. Also, the higher wind speed and structural and material

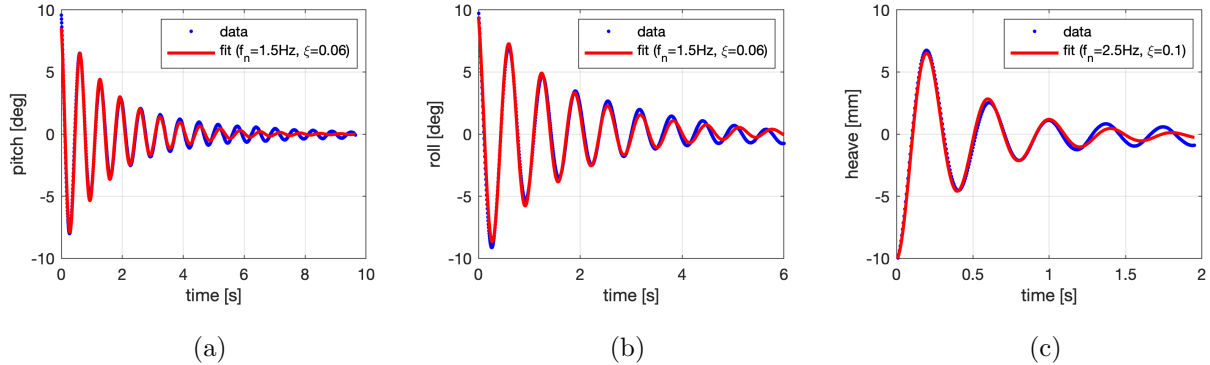


FIG. 7. Optical measurement of impulse response with no-wind, for tilt (a), roll (b) and heave (c).

354 challenges, inevitably results in a scaled model that is heavier than required by Froude
 355 scaling. Considering the force and moment ratios R1-R4 discussed in section II, the floater
 356 diameter ($D_{floaters}$) and floater spacing (L) are increased to improve the response of the
 357 scaled model. The main objective is to match the natural frequency and amplitudes for
 358 pitch, roll and heave motions to those of a full-scale turbine, as closely as possible. See
 359 appendix A for an illustration of the sensitivity of the pitch natural frequency to ballast
 360 weight and floater dimensions for a number of different floater designs. After iterating
 361 multiple designs, a final design was selected based on the measured natural frequencies,
 362 3D-printing constraints, and wind-tunnel size limitations. The final dimensions arrived at
 363 in the present study are shown in figure 6. The corresponding weight distribution and mass
 364 moment of inertia, as calculated by the CAD software are documented in table I.

365 The scaling ratios as described in section II are compared between the scaled model and
 366 the full-scale target turbine (OC5 DeepCWind platform + 60m diameter rotor) in table II.
 367 Despite the very large scaling ratio of 1:400, the ratios R1 to R4 are matched reasonably
 368 well, with average ratio of ratios of order unity. It is thus expected that this scaled model
 369 will have a similar responsiveness to wind and wave loads for surge, heave and pitch motions.

370 The natural frequency for pitch, roll and heave were measured from the free-decay impulse
 371 response with optical tracking, as shown in figure 7. Table III presents the measured natural
 372 frequency of the scaled model. The measured frequencies are also scaled to full-scale con-
 373 ditions, using the estimated hub-height velocity in the wind farm experiment $U_h = 2.9m/s$
 374 (see section VI), and the rotor diameter $D = 0.15$ m. As a reference, we mention that the
 375 pitch natural frequency of full scale semi-submersible floating wind turbines is typically in

	full-scale reference	lab-scale model	full-scale lab-scale
Rotor Diameter [m]	60	0.15	
Wind speed [m/s]	25	2.9	
CT	0.65	0.65	
Hub height [m]	43	0.113	
Total Mass [kg]	1.4×10^7	0.16	
Hydrostatic restoring moment in pitch [Nm/rad]	-1.4×10^9	-9.6×10^{-2}	
Hydrostatic restoring moment in heave [N/m]	3.8×10^6	58	
Mass moment of inertia for pitch [kgm^2]	1.6×10^{10}	6.7×10^{-4}	
R1	0.005	0.006	0.8
R2	1.6	0.9	1.7
R3	0.011	0.027	0.4
R4	0.009	0.007	1.3

TABLE II. Overview of scaling parameters compared to a reference floating wind turbine with a rotor diameter of 60m and fixed to the OC5 DeepCWind platform.

Free decay response	Measured natural frequency model [Hz]	scaled to D=60m $U_h=25m/s$ [Hz]	scaled to D=126m $U_h=25m/s$ [Hz]	Strouhal number	Damping ratio
Pitch	1.5	0.032	0.015	0.08	0.06
Roll	1.5	0.032	0.015	0.08	0.06
Heave	2.5	0.054	0.026	0.13	0.1

TABLE III. Measured natural frequency for pitch, heave and roll, from fitting the impulse response to free-decay tests.

376 the range of 0.02Hz - 0.06Hz [84–90], and is 0.035Hz for the OC5 DeepCWind turbine with
 377 NREL 5MW rotor [75]. Scaled to a full-scale turbine with diameter of 60m and for a hub
 378 wind speed of 25m/s, the model natural frequency is around 0.032Hz, and thus matches
 379 the typical range very well. Similarly, the measured heave natural frequency scaled to refer-

	full-scale reference	lab-scale model	$\frac{\text{full-scale}}{\text{lab-scale}}$
Rotor Diameter [m]	126	0.15	
Wind speed [m/s]	25	2.9	
CT	0.65	0.65	
Hub height [m]	90	0.113	
Total Mass [kg]	1.4×10^7	0.16	
Hydrostatic restoring moment in pitch [Nm/rad]	-1.4×10^9	-9.6×10^{-2}	
Hydrostatic restoring moment in heave [N/m]	3.8×10^6	58	
Mass moment of inertia for pitch [kgm^2]	1.6×10^{10}	6.7×10^{-4}	
R1	0.045	0.006	7.0
R2	7.0	0.9	7.4
R3	0.46	0.027	17.2
R4	0.040	0.007	5.9

TABLE IV. Overview of scaling parameters compared to a reference floating wind turbine with an NREL5MW rotor fixed to the OC5 DeepCWind platform.

ence turbine conditions corresponds to 0.054Hz, in agreement with the natural frequency of 0.057Hz for the OC5 DeepCWind turbine with an NREL 5MW turbine [75]. The Strouhal number corresponding to the pitch natural frequency of a full-scale turbine (i.e. a natural frequency of 0.035Hz for turbines with $D = 60\text{m}$ up to $D = 120\text{m}$ and $U_h = 6\text{m/s}$ up to $U_h = 30\text{m/s}$) can range from $St = 0.07$ up to $St = 0.7$. The pitch natural frequency Strouhal number of the scaled model $St = 0.08$ matches well compared to the reference turbine with $D = 60\text{m}$, $U_h = 25\text{m/s}$, and a natural frequency of 0.035Hz, leading to $St = 0.08$. If we extend the scaling to the OC5 DeepCWind turbine with an 126m NREL 5MW rotor, the corresponding natural frequency is 0.015Hz for pitch, which is a factor 2 smaller. Thus, for a larger rotor diameter than the target of 60m, some further adjustments to the floater design should be made. For reference, table IV presents a comparison of the dimensionless ratios with the OC5 DeepCWind turbine with NREL 5 MW rotor. In this case the R1 to R4 ratios are larger, indicating the relatively higher dimensionless inertia. As a result, compared to this larger turbine, the scaled model will have less sensitivity to smaller wind fluctuations,

394 while the dominant motions will be mostly triggered at a Strouhal natural frequency which
 395 is a factor 2 smaller. The ratios R2 and R4 represent the ratio of a dimensionless spring
 396 constant (hydrostatic restoring force or moment) over inertia (mass for R2, mass moment
 397 of inertia for R4). Making the analogy with a harmonic oscillator, the square root of these
 398 ratios links to the dimensionless natural frequency of the turbine $f_n = \sqrt{k/m}$, with k the
 399 spring constant and m the mass. The square root of the ratio of R4 is 2.4, which corre-
 400 sponds with the ratio of the OC5 DeepCwind + NREL 5MW natural frequency divided by
 401 the measured scaled natural frequency for pitch, i.e., $0.035Hz/0.015Hz \approx 2.3$.

402 In general, we conclude that by adjusting the floater design it is possible to bring the
 403 response of a scaled model closer to that of a full-scale floating turbine. As discussed in
 404 section V, for wind-only, no-wave conditions, the measurements show pitch fluctuations
 405 of $\pm 2^\circ$ around the mean, showing that the wind-driven pitch fluctuations have a similar
 406 magnitude as for full scale turbines [91].

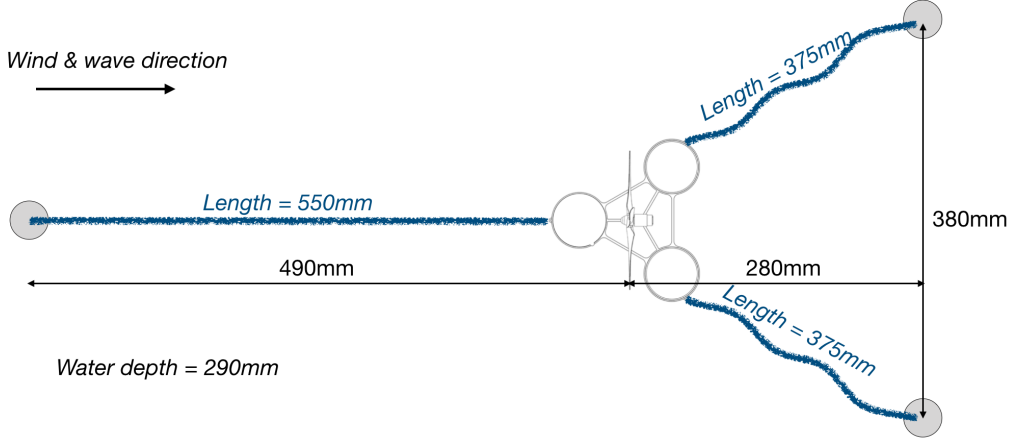


FIG. 8. Schematic of the mooring setup.

407 Floating turbines are connected to the seabed with a mooring system. Scaling the mooring
 408 system is challenging as it can strongly affect the motion of the turbine under wind and wave
 409 loading. A simple three line mooring system is used to keep the floating turbines in place,
 410 see figure 8 for the configuration using thin nylon braided wires. Optimizing the design of
 411 a scaled mooring system for a floating wind turbine experiment is left for future studies,
 412 and no scaling effort is done to match the stiffness of the mooring system at this time.
 413 The resulting motion of the moored floating turbines is measured for each condition and

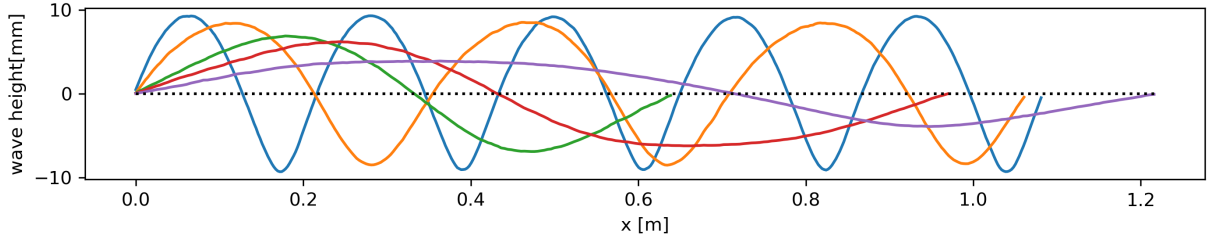


FIG. 9. Measured wave shapes for no-wind condition, projected to spatial coordinates using the measured wave velocity. The waves shapes are shown for 2.7Hz, 2.0Hz, 1.5Hz, 1.2Hz and 1Hz waves, in order from smallest to largest wave length.

⁴¹⁴ discussed in section V.

⁴¹⁵ **B. Wave conditions**

⁴¹⁶ The focus of this study is on long-period ocean waves, which have a wave period closer
⁴¹⁷ to the natural frequency for pitch and roll of a full-scale floating turbine (e.g. ocean swell
⁴¹⁸ waves with a period ranging from 15 to 20+ seconds, as compared to a typical system
⁴¹⁹ period for pitch and roll of 33 seconds, and 17.5 seconds for heave [75]). As opposed to
⁴²⁰ local wind-driven waves, long-period waves present a more idealised test condition and can
⁴²¹ be generated with a precisely controlled wave-paddle. Small scale wave-interactions, such as
⁴²² small waves created by the floater motion, and effects of water material properties such as
⁴²³ surface tension are, therefore, not critical to match in this experiment. In this study, wave
⁴²⁴ conditions are tested with a frequency below, close to, and faster than the natural frequency
⁴²⁵ of the model for pitch.

⁴²⁶ As shown in figure 5, an oscillating wave paddle is used to generate waves in the water
⁴²⁷ tank. The wave paddle is located at the entrance of the wind tunnel test section, such that
⁴²⁸ the waves move in the same direction as the wind. The wave paddle is actuated by a stepper
⁴²⁹ motor, of which the rotational speed can be controlled. Via 3D printed cams, the amplitude
⁴³⁰ of the wave paddle can be adjusted, though only one setting is used in this study for all
⁴³¹ waves. At the end of the wind tunnel test section a wave damper is located. The water
⁴³² depth is set to 0.29m such that the waves just partly roll over the wave damper, resulting
⁴³³ in minimal reflections. Leftover wave energy gets trapped behind the wave damper where it
⁴³⁴ dissipates.

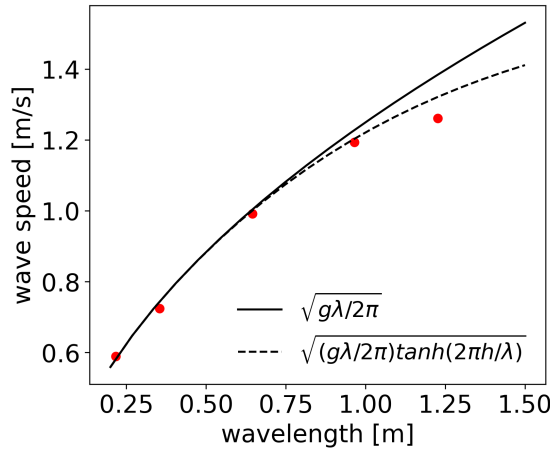
lab-scale wave measurements					full-scale equivalent		
frequency	period	length	speed	height	length	speed	height
[Hz]	[s]	[m]	[m/s]	[m]	[m]	[m/s]	[m]
2.7	0.37	0.22 (0.2Sx)	0.59	0.020 (0.13D)	87	5	8
2.0	0.49	0.35 (0.4Sx)	0.72	0.019 (0.13D)	142	6	8
1.5	0.65	0.65 (0.7Sx)	0.99	0.014 (0.1D)	258	9	6
1.2	0.81	0.97 (1.1Sx)	1.19	0.012 (0.08D)	386	10	5
1.0	0.97	1.23 (1.4Sx)	1.26	0.008 (0.05D)	490	11	3

TABLE V. Measured wave conditions in the water and wind tunnel setup. Full-scale conditions are for a wind turbine with diameter $D = 60\text{m}$ and wind speed of $U_h = 25\text{m/s}$.

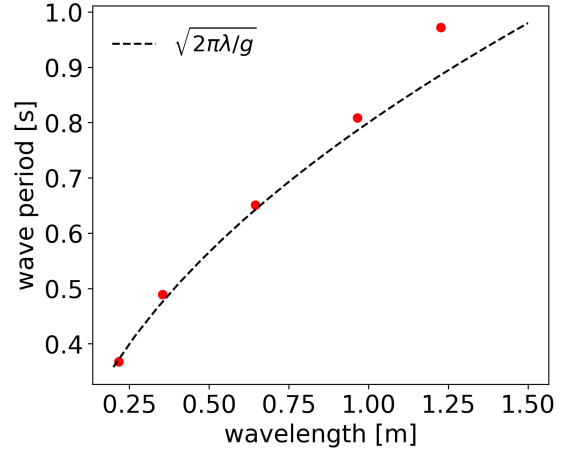
435 The wave parameters are measured using LIF (see section III A) for different frequencies
 436 of the wave paddle, corresponding to different wave periods, and for no-wind conditions.
 437 Figure 9 shows the measured wave shapes, and figure 10 shows in more detail the measured
 438 wave properties. Up to a wavelength of approximately 0.6m, the measured wave speed
 439 matches the equation for deep-water gravity waves [92], which is as expected given the
 440 water depth of 0.29m. For the wave conditions with a larger wave length, the wave velocity
 441 follows more closely the equation for transitional gravity waves [92]. The wave height reduces
 442 with wave length, and varies from 0.02m to 0.008m. Scaled to full scale conditions, these
 443 waves correspond to a wave height of 3 to 8m. Table V gives an overview of wave conditions
 444 that can be generated in the test setup.

445 Since the main objective for the experimental setup is to preserve kinematic similarity as
 446 much as possible, so that the aerodynamic effects can be studied, the ratio of wave-height
 447 and wave-length to wind turbine diameter, and the ratio of wave speed to wind speed need
 448 to be considered.

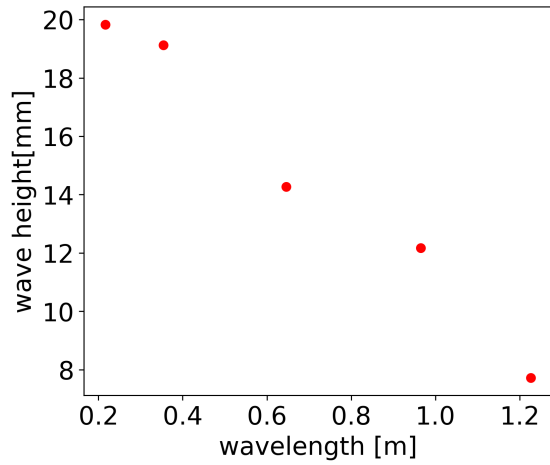
449 The PSU wave-paddle and water-tank for this wind tunnel experiment can generate waves
 450 with a wavelength of 0.2m up to 1.2m. Compared to a reference turbine with rotor diameter
 451 of 60m, these wavelengths correspond to full-scale waves with a wavelength of 87m up to
 452 490m. Deep water waves with these wave lengths, have a wave period of 7 to 17 seconds,
 453 which correspond to typical ocean wave conditions. However, due to not fulfilling Froude
 454 scaling, the wave period of the waves in the experiment is relatively larger, and the wave



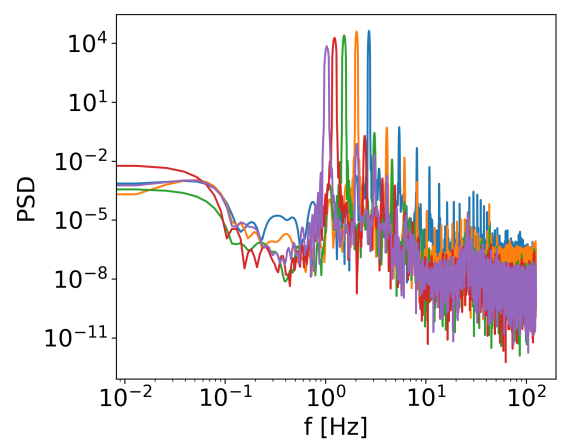
(a)



(b)



(c)



(d)

FIG. 10. Measured wave speed as a function of wave length compared to the relation according to linear wave theory for deep water waves and transitional gravity waves [92] (a), measured wave period as a function of wave length compared to the relation for deep water gravity waves [92] (b), measured wave height as a function of wavelength (c), and the power spectrum of wave height (d).

455 speeds relatively smaller. Full scale deep-water waves with a wave length of 490m have a
 456 wave speed of 28 m/s, while the wave speed in the experiment corresponds to 11 m/s in
 457 full-scale conditions. The wave speed needs to be considered when analysing the results as
 458 it can affect the spatio-temporal correlation of motion and power output among turbines in
 459 a floating wind farm. Long period waves can travel over long distances, and floating wind
 460 farms can be subject to such waves even though they are located elsewhere. Therefore, the

⁴⁶¹ ratio of wind-speed/wave-speed can be smaller than 1 as well as larger than 1 in offshore
⁴⁶² wind farms. The wave-speeds in the wind tunnel range from 0.6 m/s to 1.26 m/s, thus
⁴⁶³ limiting these tests to conditions where the wind speed is larger than the wave speed, such
⁴⁶⁴ that the Reynolds number remains sufficiently large.

⁴⁶⁵ **C. Wind farm layout**

⁴⁶⁶ The wind turbine power output in an array of turbines decreases with downstream po-
⁴⁶⁷ sition, due to superposition of wakes. Though it can take up to tens of rows of turbines to
⁴⁶⁸ reach a fully developed state [49, 93], it is generally found that after three rows of turbines,
⁴⁶⁹ the turbine power output stabilizes, i.e., it becomes independent of downstream distance
⁴⁷⁰ [46, 94]. Similarly, the flow statistics undergo the largest changes in the first few rows of
⁴⁷¹ the wind farm [72]. A wind farm with four rows and three columns of floating turbines is
⁴⁷² chosen to be scaled to the PSU wave tank, with flow measurements to be taken between the
⁴⁷³ third and last row.

⁴⁷⁴ Considering the dimensional limitations of the wind tunnel test section, a wind turbine
⁴⁷⁵ diameter of 0.15m, a streamwise spacing of $Sx/D=6$, and a spanwise spacing of Sy/D
⁴⁷⁶ = 3, are selected. The streamwise spacing is slightly less than typically used in newer
⁴⁷⁷ offshore wind farms (e.g. spacings similar to $Sx/D=7$ or larger in some cases [94]), which
⁴⁷⁸ is selected to maximize the number of rows in the available wind tunnel test section. A
⁴⁷⁹ slightly smaller spacing will in effect increase the impact of wake losses on the power output
⁴⁸⁰ of downstream turbines, which can reveal more clearly changes in wake-interactions. The
⁴⁸¹ spanwise spacing is smaller than generally used in wind farms (e.g. spacings similar to
⁴⁸² $Sy/D=5-7$ or larger in some cases [94]), which are designed for variable wind directions.
⁴⁸³ However, transverse turbulent wake spreading is slow compared to the streamwise velocity,
⁴⁸⁴ and in an atmospheric boundary layer turbine wakes usually exhibit linear wake spreading
⁴⁸⁵ with a wake-expansion coefficient on the order of $k \approx 0.08$, resulting in a wake growth
⁴⁸⁶ governed by $D_w = D + 2kx/D$. Again, a relatively smaller spanwise spacing is in effect a
⁴⁸⁷ scenario which will reveal interactions more clearly [95].

488 **D. Wind tunnel inflow**

489 The clean low-turbulence flow at the inlet of the wind tunnel test section is used without
490 active or passive turbulence grid or generators. At the start of the wind tunnel test section a
491 turbulent boundary layer will start, triggered by three plastic chains, with a height of 25mm,
492 located on the floor in perpendicular direction to the flow, and the step-change between
493 the wind tunnel floor and water height. For the experiments with a floating wind farm,
494 an internal wind farm boundary layer will develop starting from the first row of turbines.
495 Given that there is no background turbulence in the inflow, the turbulence seen by the
496 downstream turbines is thus mainly generated by wakes of upstream ones. Due to the lack
497 of a boundary layer inflow with large turbulent structures, a slower wake recovery is expected
498 for the first row of turbines, resulting in a high power drop. But, for downstream turbines,
499 the increased turbulence will result in an increased wake recovery, and thus power output.
500 We recall that generally the turbine power stabilizes quickly by the second and third row
501 [49]. The absence of a boundary layer inflow with typical very-long streamwise meandering
502 turbulent structures will reduce the correlation in power outputs between turbines due to
503 wind fluctuations. However, this allows us to focus on correlations that may result from
504 dynamic wake changes due to floating wind turbine motions.

505 **V. SCALED FLOATING WIND TURBINE TEST**

506 The scaling methodologies applied to the scaled turbine model are explored by placing a
507 single structure in the PSU wind tunnel and performing motion and power measurements for
508 different wind and wave conditions. For these tests, the incoming wind speed is measured
509 using 2-D - PIV of a streamwise-vertical plane, using a single 4M camera (see Appendix
510 A). Figure 11 (a) shows the measured velocity profiles for two different wind tunnel speeds,
511 corresponding to a free-stream velocity of $U_h = 2.2\text{m/s}$ and $U_h = 4.3\text{m/s}$, and different
512 wave conditions. The solid colored lines show the measured velocity profile for a wind-only
513 condition. Black dashed lines indicate the bottom-tip, top-tip and hub-height, showing that
514 the turbine operates mostly in the logarithmic layer of the velocity profile, up to a height
515 just below the boundary layer height. The turbulence intensity at hub height is around 10%
516 for both cases, as shown in figure 11 (b).

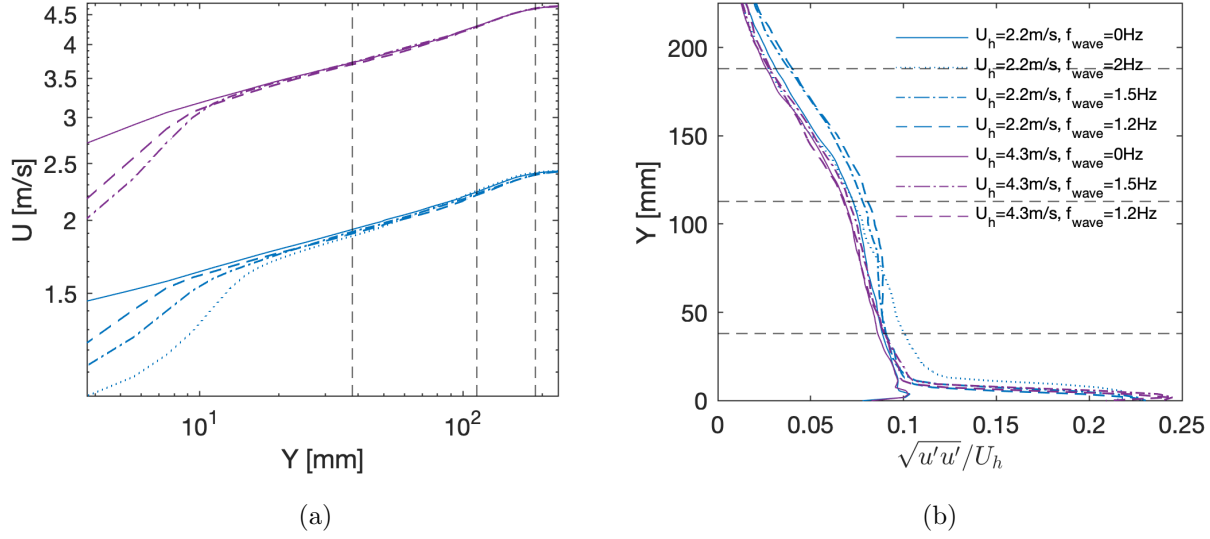


FIG. 11. The measured inflow conditions for different wave conditions used to measure the single turbine performance. The measured inflow is shown for two different wind tunnel speeds, corresponding to a free-stream velocity of 2.2m/s and 4.3m/s. Black dashed lines show the top-tip, bottom-tip and hub height on the velocity profile (a) and turbulence intensity profile (b).

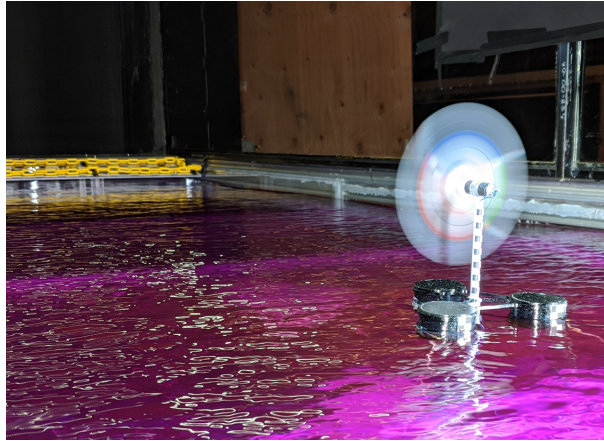


FIG. 12. Photo of a single floating wind turbine in the wind tunnel subject to 1.2Hz waves.

517 A National Instruments NI USB 6216 acquisition card is used to measure the current of
 518 the DC generator at a sampling rate of 10 kHz. The rpm of the turbine is controlled with
 519 a 200 Ohm variable resistor. The commutator signature in the current power spectrum is
 520 used to determine the rpm of the rotor. This method was first validated using a separate
 521 optical tachometer on a fixed bottom turbine during the tests by Ferčák et al. [60], and was
 522 found to be in good agreement thanks to the strong commutator signature. This spectral

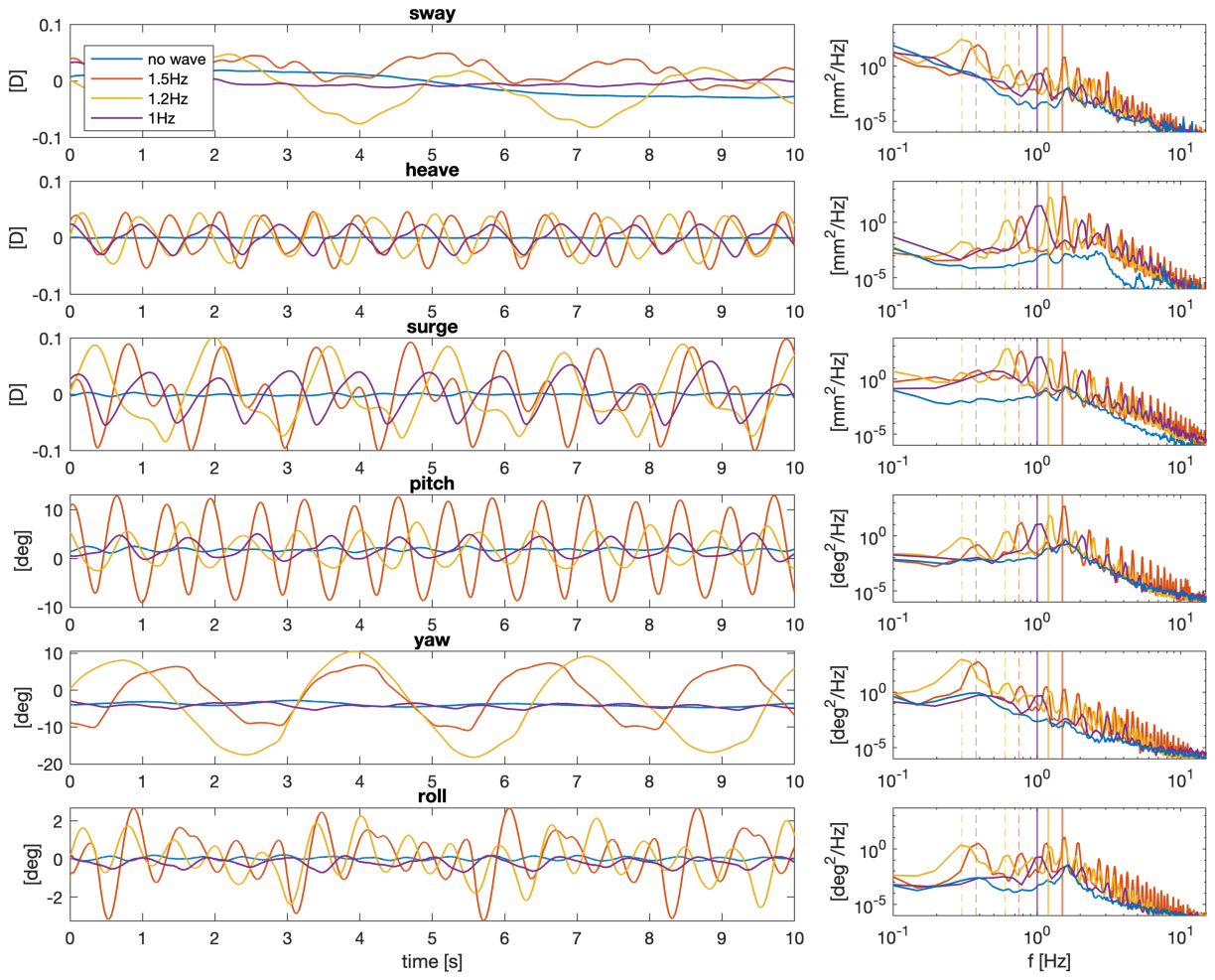


FIG. 13. Motion time trajectories of a single scaled floating wind turbine subject to a hub wind speed of 2.2m/s. Vertical colored lines in the right panels indicate the wave frequencies, and their sub-harmonics.

523 approach is found more reliable than using an optical tachometer for a floating wind turbine,
 524 because the constant motions make alignment of the sensor with the rotor unreliable. The
 525 power coefficient is measured for two wind speeds; a hub velocity of $U_h = 2.2$ m/s and
 526 $U_h = 4.3$ m/s, corresponding to Reynolds numbers of $Re_D = 2.2 \times 10^4$ and $Re_D = 4.3 \times 10^4$.

527 The motion of the floating turbine is tracked with a stereo camera configuration, as
 528 described in section III B. The measured turbine motion trajectories and corresponding
 529 power spectral density are shown in figure 13 for different wave conditions and for a tip
 530 speed ratio of approximately $TSR \approx 4.5$, which is close to optimal ($TSR = 4.8-5$, depending

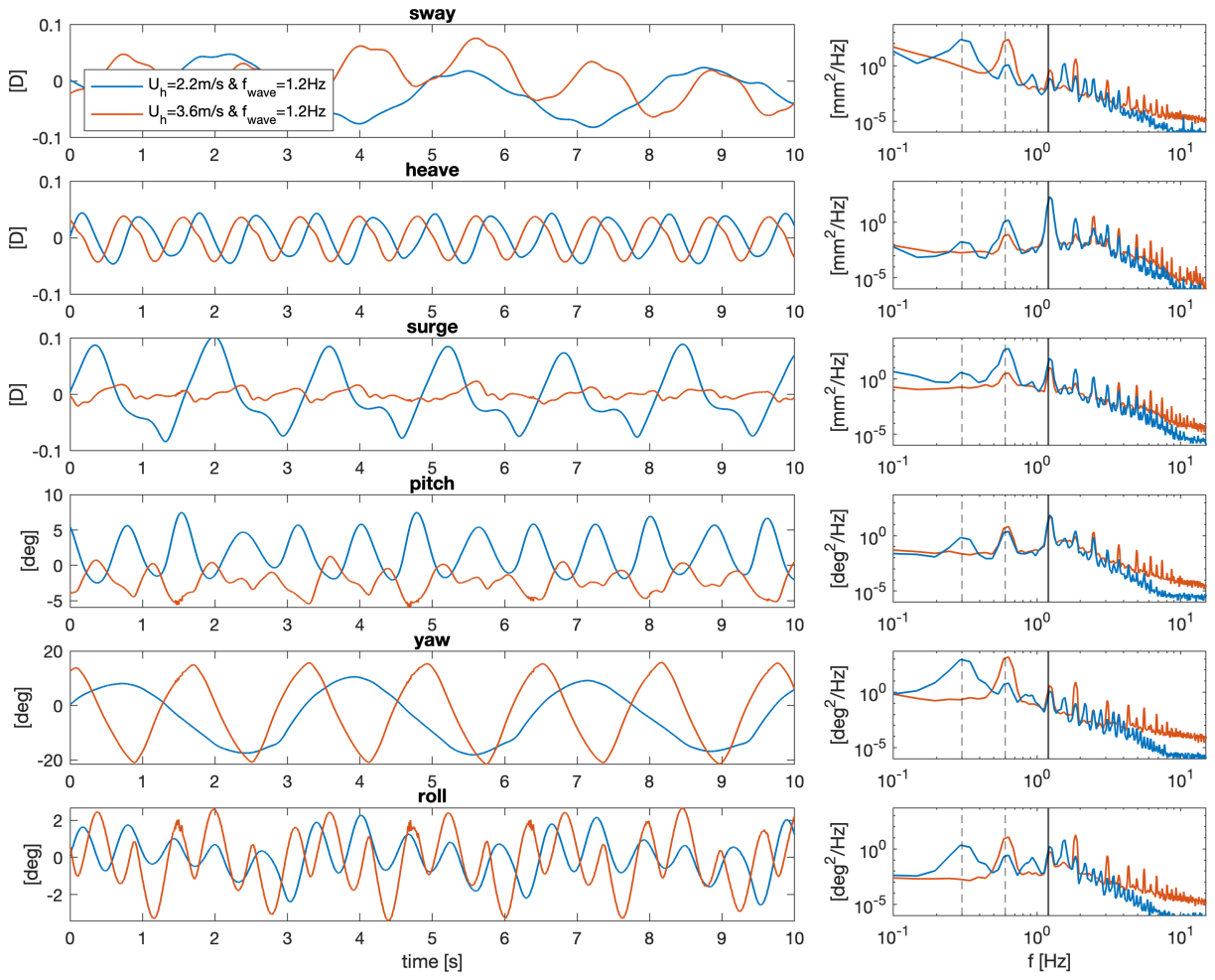


FIG. 14. Motion trajectories of a single floating wind turbine subject to a wave with frequency of 1.2Hz, and for two wind speeds. The vertical black lines in the right panels indicate the wave frequency and its sub-harmonics.

531 on the wind speed as discussed below). In the case of no wave-forcing, the motion of the
 532 floating turbine is relatively small. The pitch angle oscillates around its mean with an
 533 amplitude of $\pm 2^\circ$ for the low speed case, and $\pm 1^\circ$ for the higher speed case, indicating an
 534 effect of the mooring under higher wind loads. In comparison, tests of the DeepCWind
 535 turbine with dynamic wind loads only and for a mean hub velocity of 20m/s (in full scale
 536 conditions) measured a variation of $\pm 2^\circ$ around the mean pitch angle [84]. Long-period sway
 537 motions are measured at frequencies on the order of 0.1Hz ($St = 0.003$ to $St = 0.007$). For
 538 a wave frequency of 1.5Hz, a strong pitching motion of $\pm 10^\circ$ is present, suggesting that the

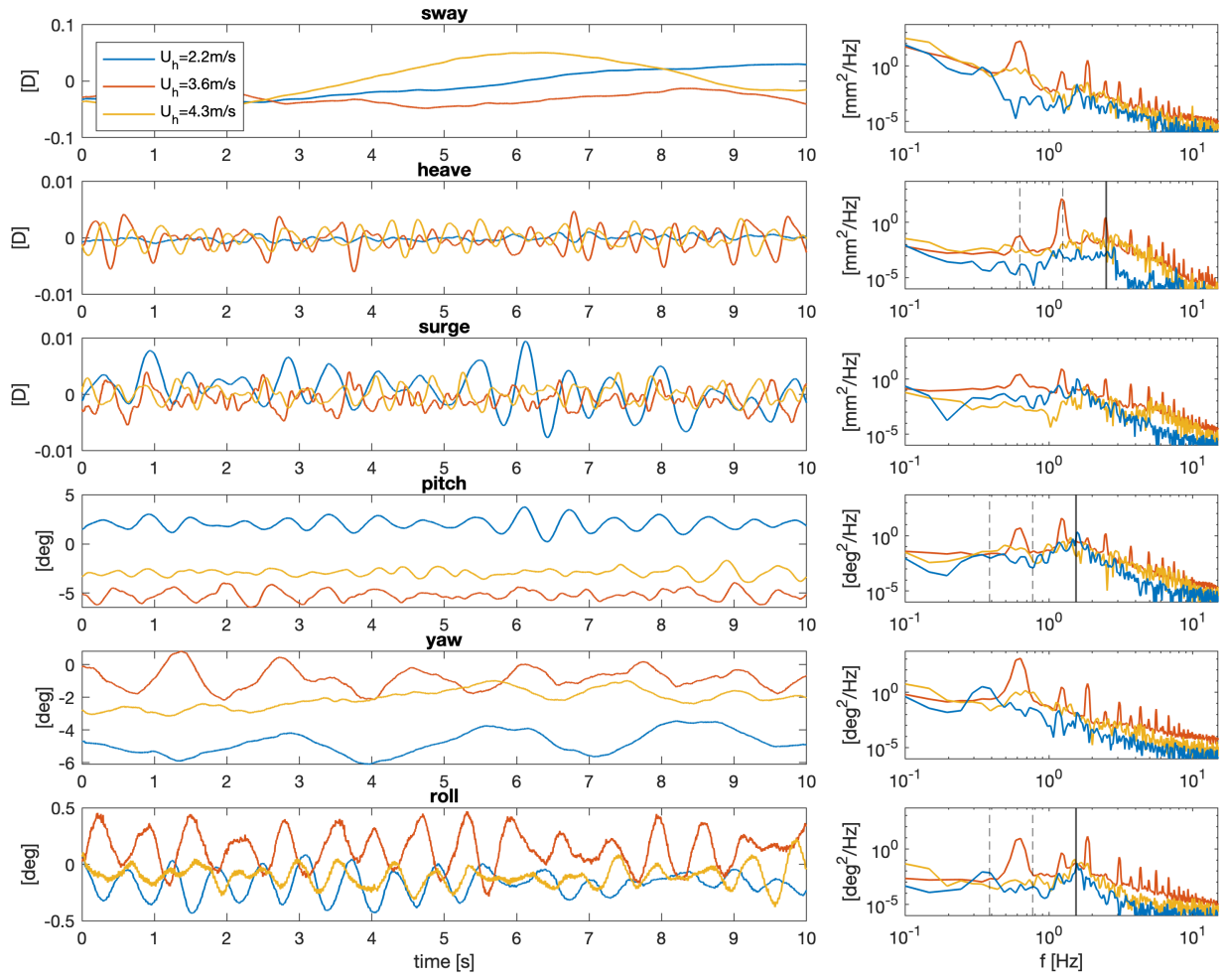


FIG. 15. Motion trajectories of a single floating wind turbine subject to no waves and for three wind speeds. The vertical black lines in the right panels indicates the natural frequency for pitch, roll or heave.

539 natural frequency for pitch is excited. A periodic yaw motion is also introduced, however,
 540 at a frequency four times smaller than the wave-frequency. Yaw motions are within -10°
 541 and $+8^\circ$. For a wave frequency of 1.2Hz, the pitching motion is reduced to $\pm 5^\circ$, but the
 542 strong yaw instability is still triggered. For comparison, Hall and Goupee [96] show pitch
 543 angles fluctuating between 0° and 8° for a full scale turbine operating in 20m/s dynamic
 544 wind and sea conditions. This indicates that the magnitudes of measured pitch angles are
 545 reasonable for extreme conditions. The periodic yaw motion is measured at a frequency of
 546 1/4th of the wave frequency. The frequency of the yaw-instability jumps to a frequency

547 of 1/2 of the wave-frequency for higher wind speeds, as shown in figure 14. Under higher
548 wind loads, the mooring makes the wind turbine response stiffer, increasing the natural
549 frequency of this yaw instability. For the low wind speed of 2.2m/s and the wave with a
550 frequency of 1Hz, the yaw instability is gone, and the pitching motion is largely reduced,
551 a clear heave motion is still present. For larger wind speeds, the yaw stability remains
552 triggered for the 1Hz wave (not shown), indicating the importance of the wind and wave
553 load balance in determining the turbine motion. In general, it is concluded that the tested
554 wave and wind conditions, together with the scaled floating wind turbine design, generate
555 a number of extreme conditions with well defined pitch, yaw, heave, sway, roll and surge
556 motions. The amplitudes of all motions are in a reasonable range (i.e. maxima of pitch up
557 to 10 degrees, sway and heave amplitudes up to 0.05D, and surge amplitudes up to 0.1D
558 [75, 97]), considering the conditions. Though some conditions result in relatively large yaw
559 misalignment angles up to 10 degrees. The wind-only and 1Hz wave condition result in
560 roll angles smaller than 0.5 degrees, in agreement with results in the literature for full scale
561 turbines [97], though for the 1.5Hz and 1.2Hz larger values up to 2 degrees are observed
562 triggered by the large yaw motions.

563 Figure 15 shows the measured motion for three different wind speeds, with no external
564 wave generation. The results show a sensitivity of turbine motion to the incoming wind
565 speed. A higher wind load results in a larger mean pitch angle. The pitch of the turbine at
566 the lowest wind speed indicates a slight forward leaning of the turbines, as the floater ballast
567 is selected for a higher wind speed, and there is no active re-balancing. For the lowest wind
568 speed, the motion fluctuations are generally smaller, except for pitch, which is triggered at
569 the natural frequency of the model. For the higher wind speeds, the pitch natural frequency
570 is not as strongly triggered, which indicates the effect of higher tension on the mooring lines.
571 The hub velocity of 3.6m/s triggers a strong heave, pitch, and yaw fluctuation at multiples
572 of the heave natural frequency, not seen for the other wind speeds. The motions are thus
573 wind load sensitive.

574 The power spectra of turbine motion (the right panels of figure 15) show distinct peaks
575 at the wave frequencies. There are also peaks at multiples of the excitation wave frequency.
576 Motion frequency peaks go as low as $1/4^{th}$ of the wave frequency for sway, yaw and roll.
577 Higher order harmonics are visible up to 10Hz. The Strouhal number of the wave excitation
578 ranges from 0.05 to 0.08 (if scaled with the hub height wind speed ($U_h = 2.7$ m/s) in the

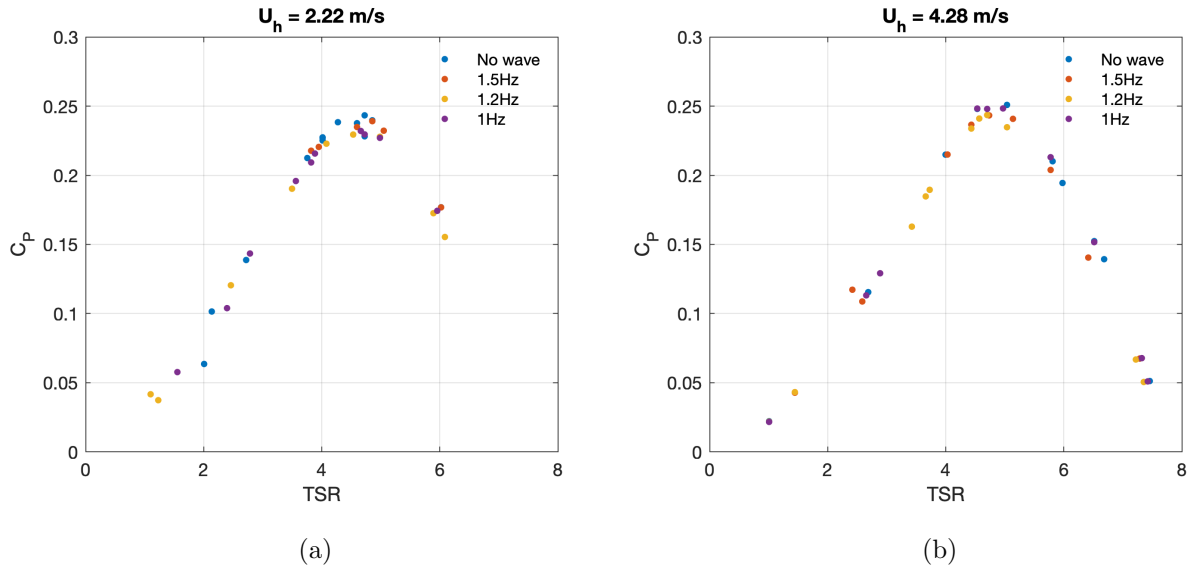


FIG. 16. The measured power coefficient for different wave paddle conditions, and for a hub wind speed of 2.2m/s (a) and 4.3m/s (b). The wave excitation period is indicated in the legend.

579 final wind farm experiment). But due to the higher order harmonics, smaller amplitude
 580 motions are present up to a Strouhal number of $S_t \approx 0.5$.

581 The power of the floating turbine is measured for a range of tip speed ratios, wind speeds,
 582 and wave conditions. For each condition, the electric power is measured for a duration of 30
 583 seconds. Simultaneously, and synchronized, the motion of the turbine is tracked. Figure 16
 584 shows the resulting measured power coefficients as a function of tip speed ratio. For a hub
 585 velocity of 4.3m/s, the maximum power coefficient is $C_p = 0.25$, and is reached at a tip speed
 586 ratio of $TSR = 5$, as shown in figure 16. For the lower wind speed of 2.2m/s, the power
 587 coefficient is slightly smaller ($C_p = 0.24$) and is reached at a slightly lower tip speed ratio
 588 ($TSR=4.7$). For the purpose of these tests, the power coefficient differences are small enough
 589 to conclude that turbine operation is Reynolds number independent for the range of inflow
 590 velocities. Interestingly, though large misalignments are observed in the tracked motion, the
 591 measured power coefficient shows only a small sensitivity to the wave conditions. However,
 592 for the lower wind speed, the power coefficient shows differences between wave conditions,
 593 at the point of maximum power.

594 Figure 17 shows the power spectrum of the motor current signal measured for a hub wind
 595 speed of $y_h = 2.2\text{m/s}$ ($TSR=3.9$), and for a hub wind speed of $y_h = 4.3\text{m/s}$ ($TSR=4.5$).
 596 Vertical dotted lines indicate the wave periods. It is clear that for a wave frequency of

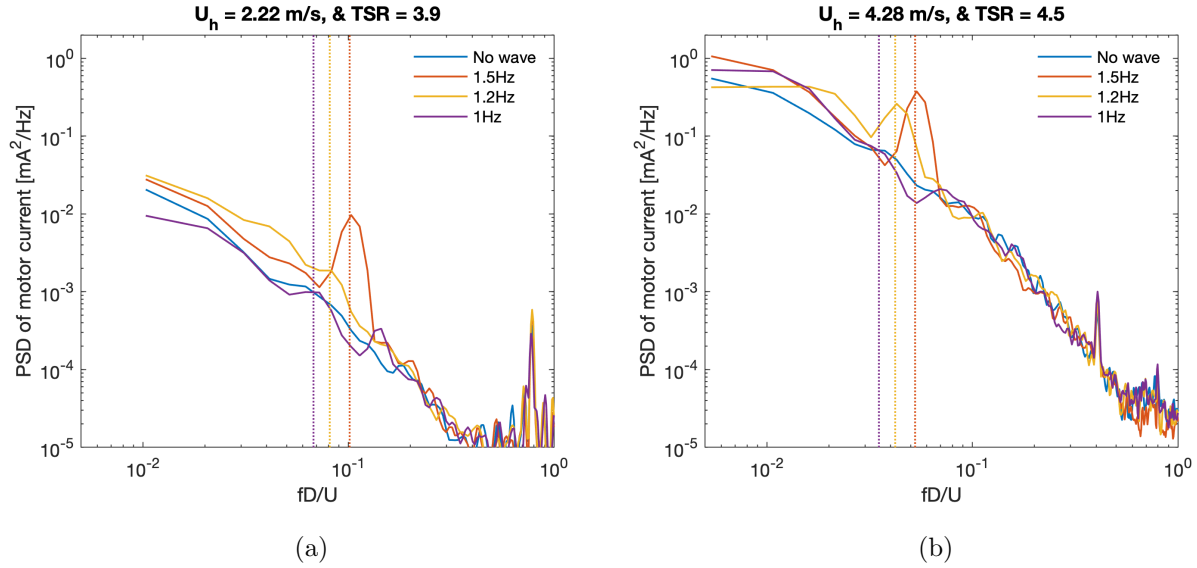


FIG. 17. Power spectral density of measured motor current for a single floating turbine subject to different wave paddle conditions, and for a hub wind speed of 2.2m/s (a), and 4.3m/s (b). The wave excitation period is indicated in the legend.

597 1.5Hz, exactly at the pitch-natural frequency of the model, a strong peak shows up in the
 598 spectrum due to the pitching motion. In the no-wave condition, the pitch natural frequency
 599 of the floating turbine is still excited by the wind fluctuations, yet a peak in the power-
 600 spectrum is not clearly seen. For a wave frequency of 1.2Hz, a peak becomes visible in the
 601 spectrum of the power output. This peak is much stronger for the higher-wind speed case
 602 ($U_h = 4.3\text{m/s}$), which is likely related to faster yaw-oscillation. Spectral peaks at higher
 603 frequencies ($St > 0.5$) are not considered as they are expected to have an electric origin
 604 related to the DC generator, instead of being related to flow or turbine dynamics. It is
 605 concluded that even though significant dynamic misalignments are observed for the floating
 606 wind turbine subject to different wind and wave loads, the power coefficient is relatively
 607 stable.

608 VI. SCALED FLOATING WIND FARM EXPERIMENT

609 Experiments are performed for a floating wind farm consisting of 12 scaled floating tur-
 610 bines (4 rows and 3 columns), to study wind-wave-wake-turbine interactions for different
 611 wave conditions, see section IV C for more information about the experiment and wind farm

612 layout. The wake properties, and motion characteristics of the middle turbine in the third
613 row are measured with S-PIV (see section A), and optical tracking (section III B). The opti-
614 cal tracking is performed separately from the PIV measurement, in order to provide enough
615 light for the tracking. All experiments are performed for four different wave conditions: no
616 external wave forcing, and a wave frequency of 1.5Hz, 1.2Hz, and 1Hz. See table V for
617 more information about the wave conditions. A single wind tunnel speed is used for all tests
618 discussed in this section. The electrical power of the middle turbine in each row is acquired
619 simultaneously for each test condition. The free stream velocity measured in a cross plane
620 at a streamwise position of $x/D = 3$ behind the middle turbine in the third row is 4.1 m/s,
621 calculated as the horizontally averaged velocity at the top of the PIV measurement window.
622 The incoming hub height velocity for the middle turbine in the third row is estimated to
623 be 2.9 m/s, based on the measured turbine power and power coefficient (as shown in figure
624 16). The tip speed ratio (TSR) of the floating turbines are tuned in the no-wave condition,
625 assuming that the turbine would operate under a classic greedy control approach so that
626 the optimal TSR is maintained. Practically, this is implemented by optimizing the tip speed
627 ratio of each turbine by changing the electrical resistor until maximum power is reached as
628 calculated from the measured current (used to estimate motor torque) and rotational fre-
629 quency (calculated from the commutator signature in the spectrum of the motor current).
630 The turbines are tuned in order of row number, starting with the first row. In this section
631 the measured motion of the turbine is first presented, followed by a discussion of the wake
632 and power output measurements.

633 A. Measured motion within scaled wind farm

634 For each S-PIV measurement, a separate test is done to measure the motion of the
635 floating turbine in the middle of row 3, using the setup described in section III B. During
636 these tests, the two cameras for tracking are positioned inside the wind tunnel, see figure
637 18. While the fourth (and last) row of turbines are not needed for this measurement, it
638 is noted that they operate in partial wake of the camera mount, which is positioned just
639 above the water surface. The last row of turbines and the cameras are assumed to have no
640 or minimal upstream effect on the motion of the turbines in the third row, as the cameras
641 are positioned five turbine diameters downstream.

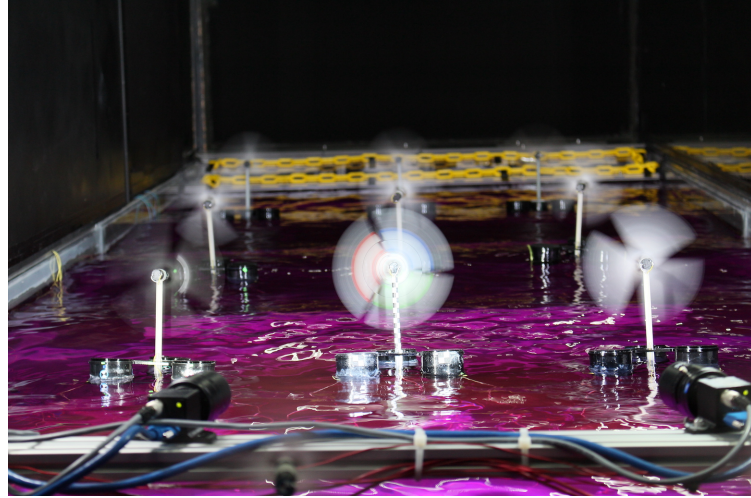


FIG. 18. Photo of the optical tracking camera setup in the wind tunnel with the floating wind farm.

642 Figure 19 shows the measured motion for the six degrees of freedom, and the correspond-
 643 ing power spectra. There are some differences in comparison to the measurements for a
 644 single turbine in figure 13, which is expected to be related to a higher wind speed during
 645 the wind farm tests (a hub-height velocity of 2.9m/s compared to 2.2m/s), and increased
 646 wake turbulence inside the wind farm.

647 Similar to the previous conclusion for a single scaled floating turbine, the yaw instability
 648 frequency in waves of 1.2Hz is higher when subject to a higher wind speed (e.g. it is found
 649 to be around $1/2 f_{wave}$ instead of $1/4 f_{wave}$). The higher wind speed directly impacts the
 650 sway and roll motion as well. The 1.5Hz waves do not trigger the yaw instability, but it
 651 is present for the wave condition of 1Hz. The amount of yaw misalignment when the yaw
 652 instability is triggered, depends on the mooring. The measurements show a higher amplitude
 653 in yaw misalignment for the wind farm measurements, which is likely due to a slightly looser
 654 mooring. It is also important to note that the mean yaw angle is around 5 degrees for all
 655 wave conditions. It is hypothesized that this is triggered by partial wake overlap, which
 656 results in asymmetric inflow conditions, resulting in a non-uniform wind loading pushing
 657 the floating turbine towards a slightly yawed position.

658 It is concluded that each wave condition results in different and strongly pronounced
 659 turbine motions. For example, the no wave condition results in a pitch fluctuation of around
 660 $\pm 2^\circ$ at the natural frequency of the turbine, but also longer period sway variations. The

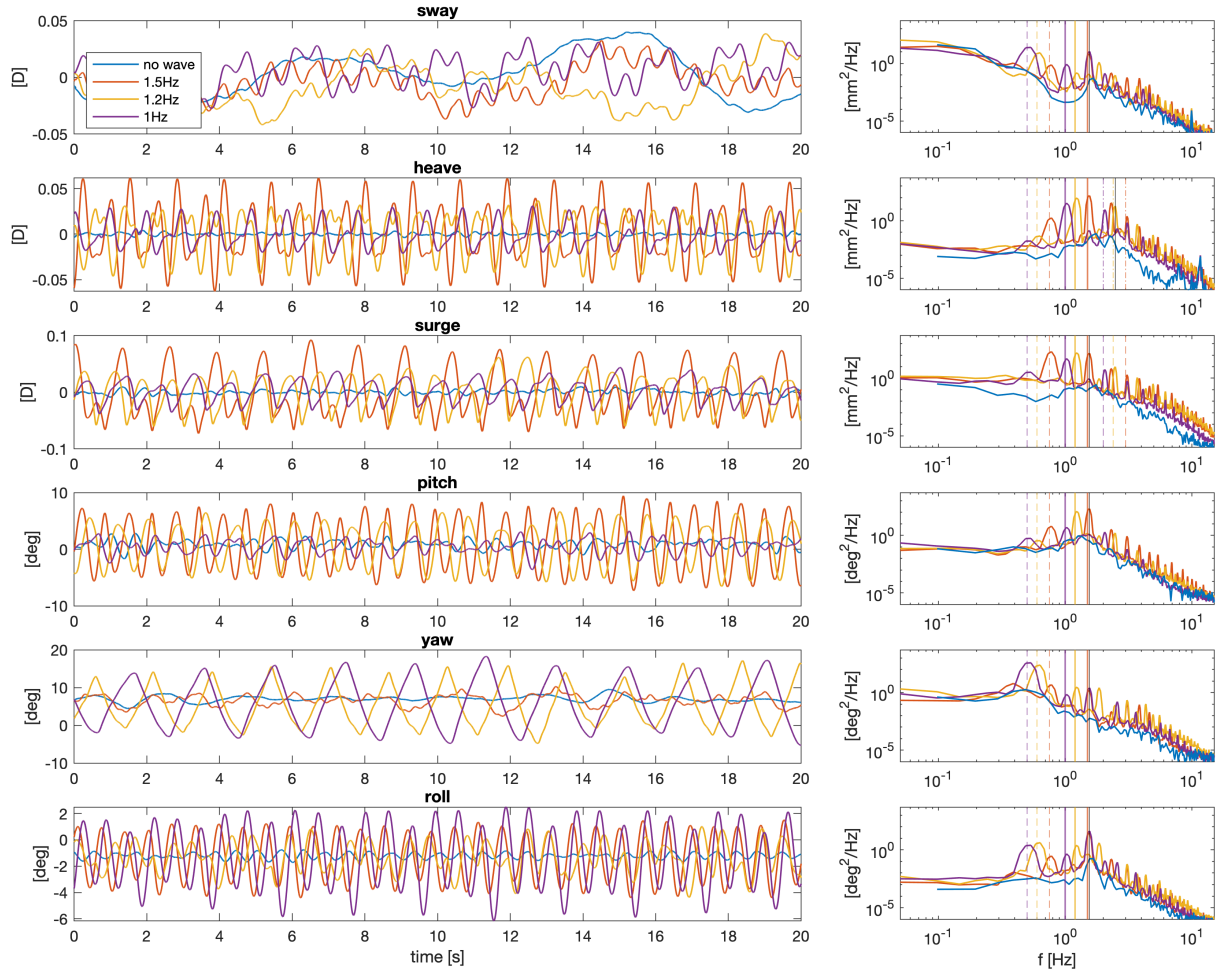


FIG. 19. Measured motion of the floating wind turbine model in the third row of the wind farm, for all four wave conditions.

661 1.5Hz wave condition results in very strong pitch oscillations, which send the wake up and
 662 down periodically, and is coupled to relatively high waves traveling through the wind farm.
 663 The 1.2Hz wave condition on the other hand leads to a scenario in which the yaw instability is
 664 the most pronounced motion of the turbine, deflecting the wake left and right periodically,
 665 although there are still significant synchronized pitch motions. The 1Hz wave condition
 666 simulates very long period ocean waves, triggering the yaw instability at a lower frequency
 667 without significant pitch motions.

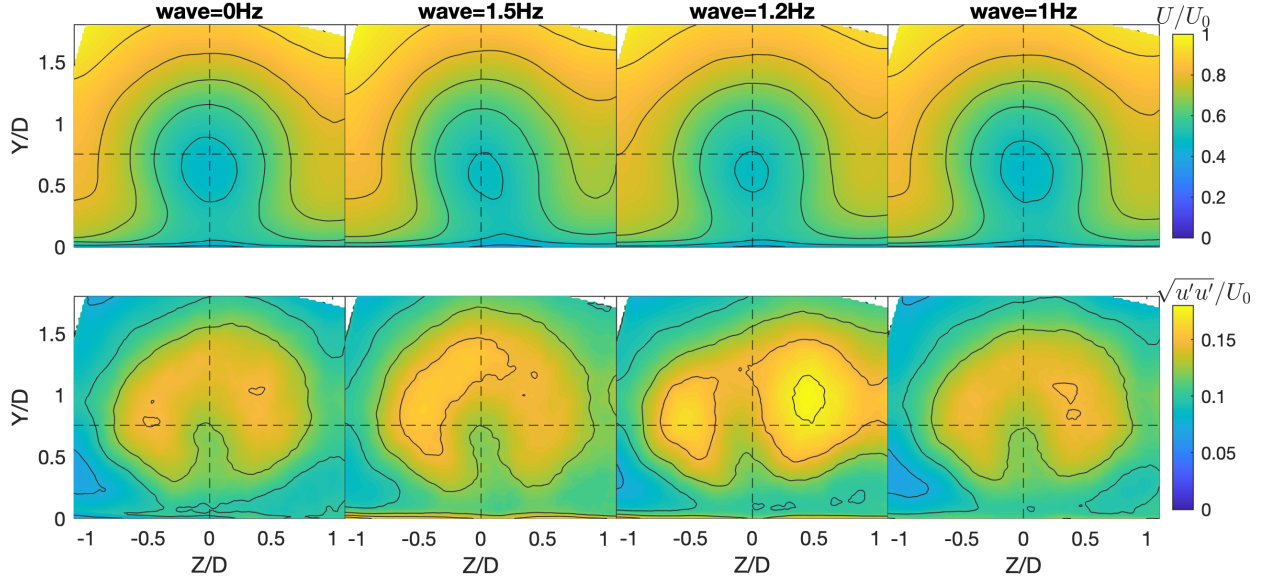


FIG. 20. Mean contours of wake velocity (top) and turbulence intensity (bottom) for all four wave conditions.

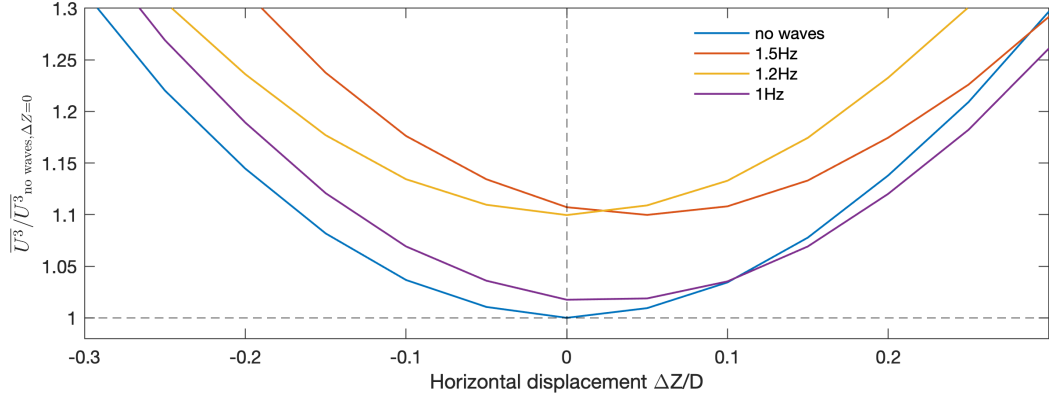


FIG. 21. Relative wake power potential as calculated by the average of U^3 over a rotor area with spanwise position ΔZ compared to the upstream turbine.

668 **B. PIV wake-measurements**

669 In this section S-PIV measurements of the wake of the middle turbine in the third row are
 670 presented. The measurements are performed at a downstream distance of $x/D = 3$ from the
 671 third-row turbine. 5000 snapshots are acquired for each condition and are averaged to cal-

672 culate distributions of mean wind velocity and turbulence intensity based on the streamwise
673 velocity fluctuation variance. The mean velocity contours are shown in figure 20, indicating
674 subtle differences in wake recovery (velocity deficit), shape, and the location of maximum
675 velocity deficit. The wakes for the 1.5Hz and 1.2Hz wave conditions show the highest mean
676 velocities and lowest wake velocities defects near the wake center.

677 In order to quantify the subtle velocity differences in terms relevant for power generation,
678 we place a hypothetical wind turbine at various locations. The change in available power in
679 the wake is estimated by spatially averaging of U^3 over different hypothetical downstream
680 rotor areas. Specifically, the effect of the spanwise position $\Delta z/D$ of a hypothetical wind
681 turbine placed at the $x/D = 3$ downstream plane is studied, and its performance is compared
682 to the aligned case with $\Delta z/D = 0$. The available power found for different wave conditions
683 and spanwise shifts is normalised by the available power for the condition with no external
684 waves and no spanwise shift (figure 21). For the condition with no external waves a spanwise
685 shift of 0.2D (i.e. going from full to partial wake overlap) can lead to an increase in power
686 of almost 15%. For the 1.5Hz and 1.2Hz wave conditions, the available power increases by
687 10% even for the case with no spanwise shift, clearly showing an impact of turbine motions
688 and wave interactions on wake recovery in a wind farm boundary layer. These values are
689 overestimates of the actual expected differences since an $x/D = 3$ downstream distance is
690 lower than spacings in typical wind farms, but the trends are instructive nonetheless.

691 In figure 20, the contours of streamwise turbulence intensity $\sqrt{u'u'}/U_0$ show distinct
692 differences between wave conditions. Zones of high turbulence intensity highlight where
693 there is high production of turbulence in the top and side shear layers of the wake, but also
694 zones where wake meandering triggered by turbine motions results in velocity variations over
695 longer time periods. The turbulence intensity contour for a wave of 1.5Hz shows stronger
696 turbulence levels at the top of the wake, possibly resulting from the periodic up and down
697 deflection of the wake. The strongest difference is seen for the 1.2Hz wave condition. In
698 this case, the wake width has increased, as indicated by the two pronounced zones of high
699 turbulence intensity on the left and right sides of the wake. This pattern is consistent with
700 a periodic horizontal deflection of the wake caused by the yaw instability. Though the yaw
701 instability is also recorded for the 1Hz wave condition, the turbulence intensity contours
702 don't show the same shape. A difference between the 1Hz and 1.2Hz scenario is that the
703 yaw motion for the case of 1Hz waves happens at a slower frequency and the pitching motion

704 is significantly reduced. The significant difference in the wake properties between the 1.2Hz
705 and 1Hz waves highlight a potential sensitivity to the Strouhal number of rotor motions, as
706 discussed by Messmer et al. [25].

707 To better understand the periodic wake behavior, the PIV results are conditionally av-
708 eraged with the wave phase at the time of each PIV snapshot. This is practically done by
709 considering the fixed frequency of the laser pulses (i.e. 3.75Hz), and fixed wave frequency of
710 the wave-paddle. Based on the acquisition time of each PIV snapshot and the wave period,
711 all snapshots are projected on to a single or double wave period, depending on the motion of
712 the turbine that is considered. Projecting the PIV measured wave heights is very sensitive
713 to the exact wave frequency. An optimization was performed to refine the wave frequency
714 for optimal synchronization with the PIV results. The refined wave frequencies show small
715 deviations from the controlled wave frequency (e.g. 1.54Hz instead of 1.5Hz), which can be
716 explained by inaccuracies in the clock frequency of the Arduino used to control the wave-
717 paddle, compared to the highly accurate timing module for the PIV measurements. Figure
718 22 shows the reconstructed wave shapes by projecting the mean water height in each PIV
719 snapshot. The synchronization frequencies are indicated for each wave condition. In general
720 very good agreement is found with the measured wave shapes captured using time-resolved
721 LIF, as shown in figure 9, though now there is more variation in wave height due to a small
722 wave-to-wave variation, and small wind effects on the water-surface. The wave period is
723 then divided in 8 phase-bins, and for each phase the PIV snapshots are ensemble averaged,
724 resulting in a conditional average of the wake contour for that specific wave phase. The
725 number of PIV snapshots in each phase-bin is about 625.

726 Figure 22 (a) shows the conditionally averaged mean velocity contours for a 1.5Hz wave
727 condition, triggering strong pitching motions. Wave phases are labeled 1-8 from bottom to
728 top of the figures. Consistent with the discussion above, the contour plots indicate an up-
729 and-down motion of the wake center at the frequency of the wave. For example, during phase
730 4 and 5, a moment of high wave height occurs at the same time and place as where the wake
731 is deflected downwards, which can be seen from the location of maximum velocity deficit
732 (indicated by a red dot) reaching a minimum height in comparison to the other phases. Due
733 to the difference in wave and wind speed, the interaction between the periodically downwards
734 deflected wake and the traveling waves will vary spatially and temporally. Figure 22 (b)
735 shows the conditionally averaged mean velocity contours for the 1.2 Hz wave conditions,

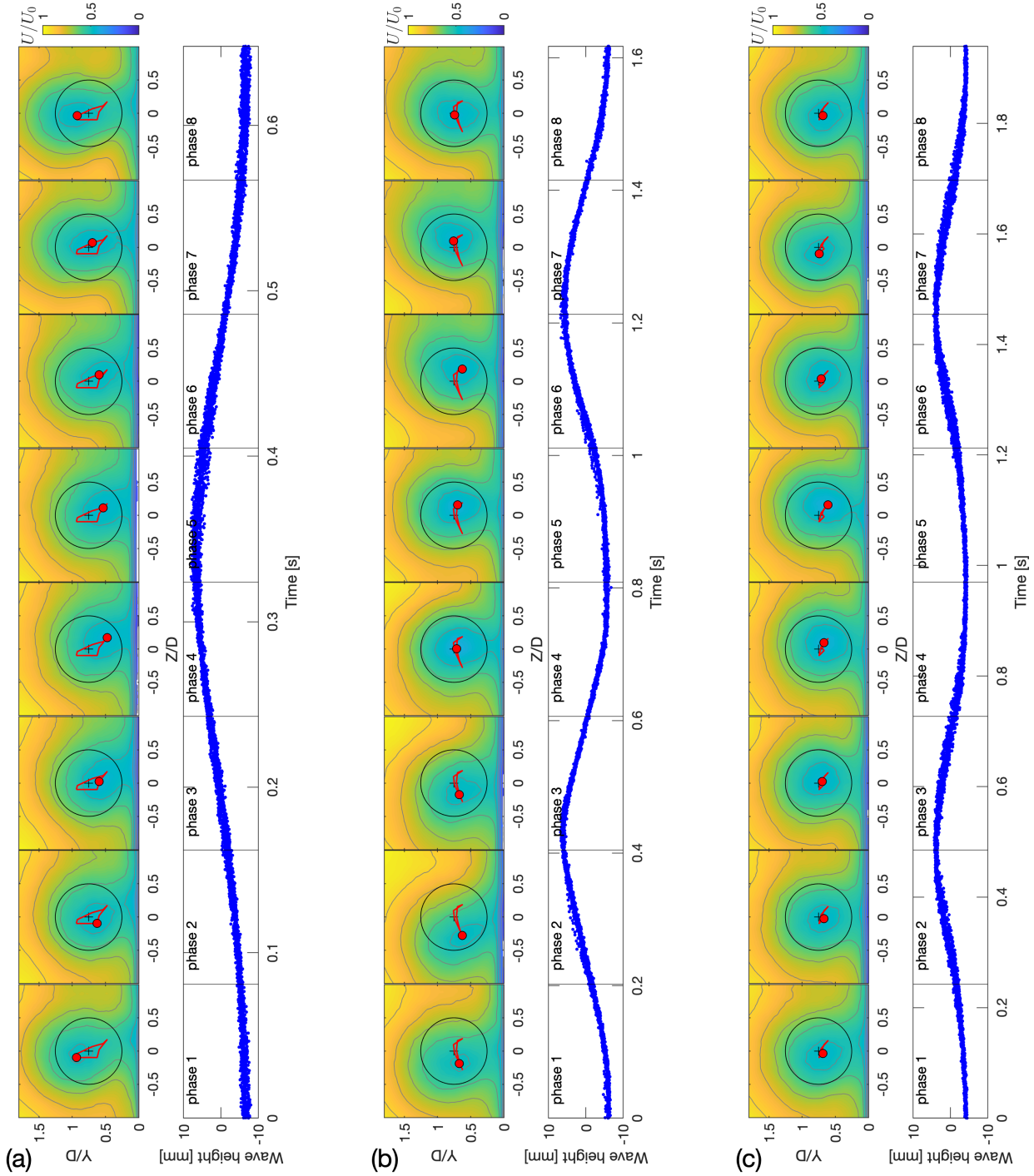


FIG. 22. Conditional averages of wake phases for 1.5Hz (a), 1.2Hz (b) and 1 Hz (c) waves, accompanied with a plot of wave height reconstructed from all PIV snapshots, projected onto a single (a) or double (b,c) wave period using a synchronization frequency of 1.5437Hz (a), 1.23647Hz (b), and 1.03116Hz (c). The maximum velocity deficit is indicated with a red dot, and its trajectory by a red contour line. The reference rotor position is indicated by a black circle to indicate wake changes.

736 triggering a strong horizontal oscillation at half the wave frequency (i.e. the wake moves
737 left and right once within the two-wave-period window), accompanied by a smaller vertical
738 oscillation at the wave frequency (i.e. the wake center moves up and down for every wave
739 period). The motion measurements also showed that for this wave condition the turbine
740 moves with a yaw oscillation at half the wave frequency, and a pitch oscillation at the
741 wave frequency. Therefore, it is clear that the conditionally averaged wake contours show
742 wake deflection from turbine misalignment which is synchronized with (and triggered by)
743 the waves. Consequently, these wave conditions show a strong left and right deflection of
744 the wake center at different wave-phases at the location of the PIV measurement plane.
745 Since the yaw and pitch oscillations happen at multiples of the wave frequency, they are
746 synchronized with one another. The moment of maximum upwards wake deflection happens
747 at a moment of minimal yaw misalignment (i.e. phases 4 and 8). The moments of maximum
748 yaw deflection are seen for phase 2 and 6, corresponding to a phase in which the wave
749 almost reaches its maximum wave height. Figure 22 (c) shows the conditionally averaged
750 mean velocity contours for the 1 Hz wave, which also results in a strong yaw oscillation, but
751 with weaker pitching motion. It is noticed that the yaw deflection is smaller, explaining why
752 the mean turbulence intensity contour in figure 20 is more similar to that of the no wave
753 condition.

754 C. Floating wind farm power output

755 In this section the spectral features of the power output of each individual turbine, and
756 of the aggregated power are investigated. Figure 23 shows the power spectral density of
757 the measured power for each row. The power signals are normalised by their mean value:
758 $P_{row,i}/\bar{P}_{row,i}$ before calculating the power spectral density. The power characteristics of the
759 first row differ from the other three rows, due to the different inflow conditions: a higher
760 inflow velocity with minimal turbulence levels. The other (downstream) rows operate in
761 waked conditions, for which the velocity is reduced, and turbulence has increased. Knowing
762 the power coefficient from the single turbine calibration, the incoming hub height velocity
763 can be estimated. The reconstructed hub height wind speeds for no wave conditions are
764 estimated to be 3.9m/s for the first row, 2.6m/s for the second row, 2.9 m/s for the third row,
765 and 2.5m/s for the last row. The spectrum of the power output is a result of the incoming

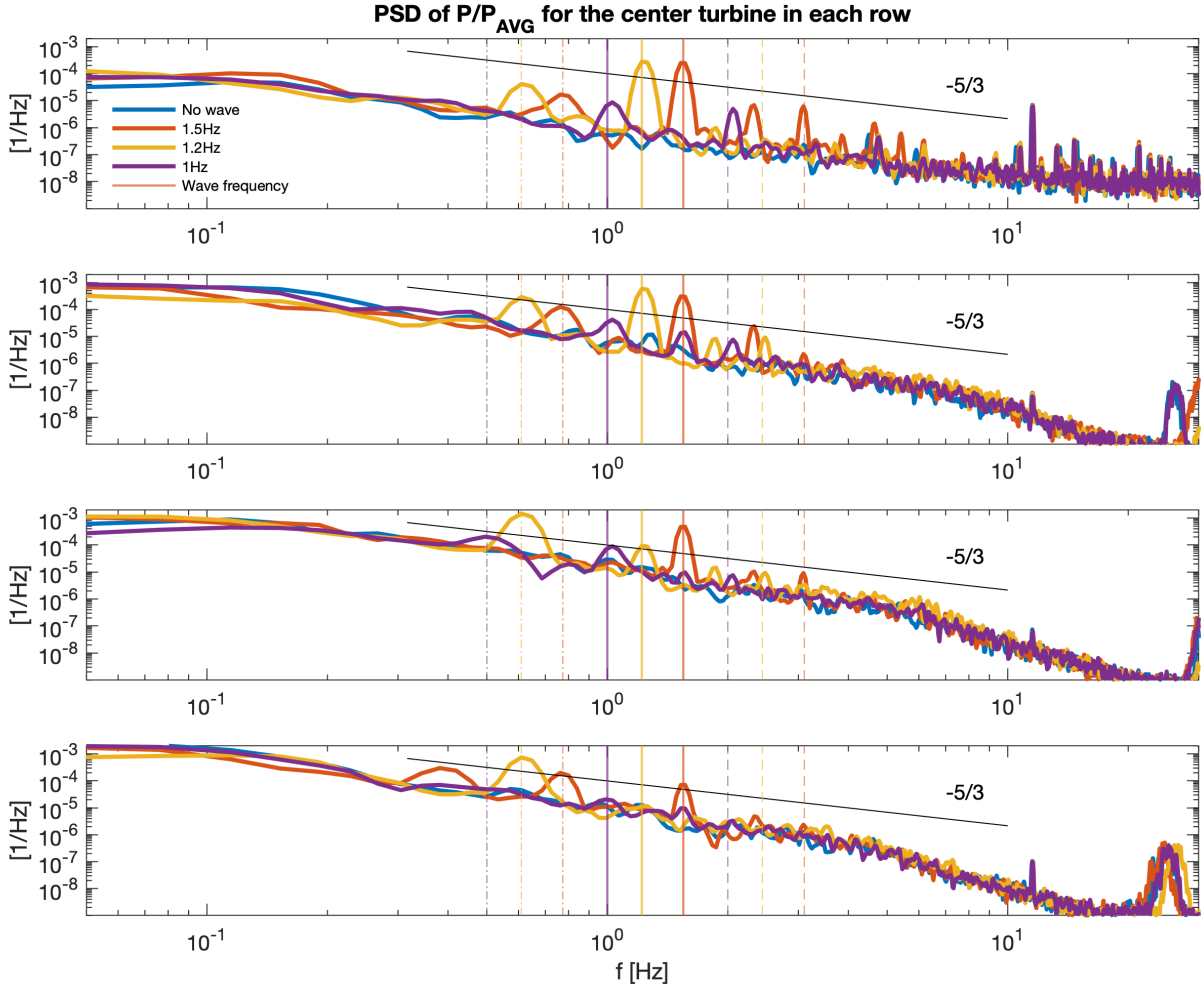


FIG. 23. Power spectrum of turbine power normalized by its time-average (P_i/\bar{P}_i) for the middle turbine in row 1 - 4, from top to bottom. Vertical lines indicate the wave frequencies (—), their second harmonic (— —) and sub-harmonic (— · —).

766 wind fluctuations and the wave oscillations. Given that for the first row, turbulence levels
 767 are low, the spectrum is mostly determined by wave oscillations. The spectra show a clear
 768 peak at the 1.5 and 1.2 Hz wave frequency. For the 1Hz waves, the peak is less pronounced,
 769 which is expected due to the more subtle motions of the turbines in these conditions. The
 770 1.2Hz wave conditions show a spectral peak at half the wave frequency due to the periodic
 771 yaw motion. For the 1.5Hz wave condition, a peak at half the wave frequency appears in the
 772 spectrum for the first, second, and last row turbines. It is not clear if this motion is a result
 773 of wind speed dependence or small changes in the mooring tension. Because the motion of
 774 turbines in the other rows was not measured, this observation cannot be confirmed. For all

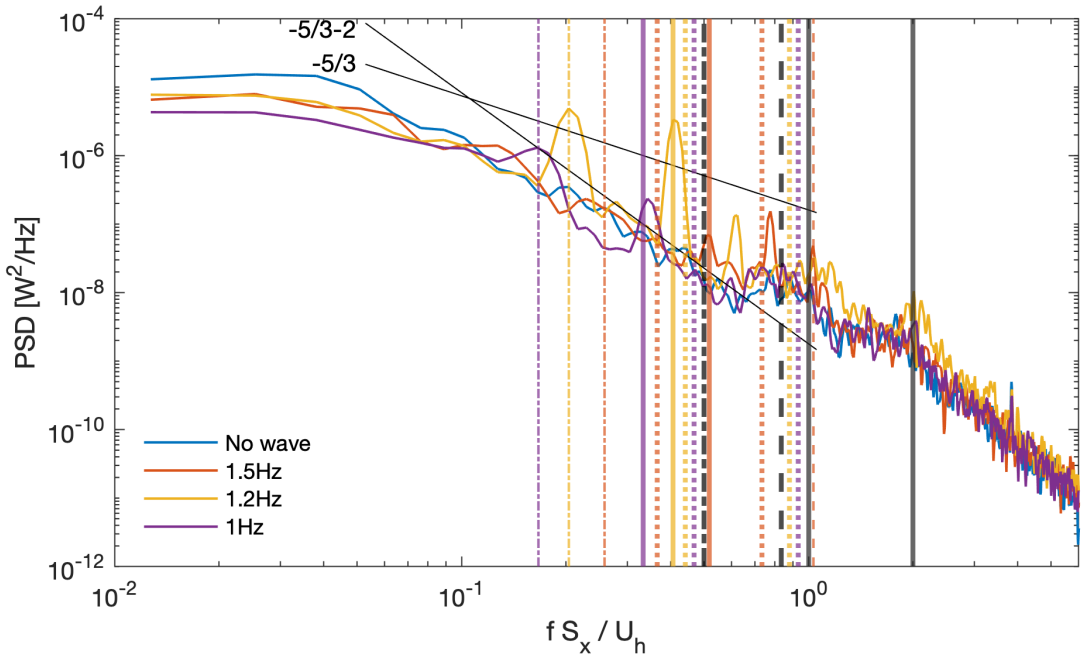


FIG. 24. Power spectrum of aggregate power of the three middle turbines in row 2, 3 and 4. Black lines indicate: the flow-convective frequency corresponding to one and two turbine spacings S_x (—), the natural frequency for heave (---), and the natural frequency for pitch (—.). Colored lines indicate the wave excitation frequencies (—), half of the wave frequency (—.), double the wave frequency (——), and the frequency related to wave speed and turbine spacing S_x/v (.:).

rows, the 1.5Hz and 1Hz wave conditions result in a distinct spectral peak of the power at the first harmonic, corresponding to double the wave frequency. For the 1.5Hz wave condition, a spectral peak at the natural frequency for heave (2.5Hz) is noticed in the power spectrum of rows 1 and 2. The spectral peak at the wave frequency for the 1.5Hz waves is present in the power output of every row, confirming the high sensitivity of turbine power to pitching motions. The spectral peak at the wave frequency for a 1.2Hz wave becomes smaller with increasing row number.

Figure 24 shows the power spectrum of the combined wind farm power of the center turbine in rows 2, 3, and 4. The turbine in row 1 is left out of this aggregate because it is subject to different inflow conditions with a higher wind speed and minimal turbulence levels, and here we aim to study specifically turbulent wind farm conditions. Including row 1 does not drastically change the behavior, though it may obscure possible spatial-temporal correlations due to coherent turbulent structures. The power spectrum of the combined

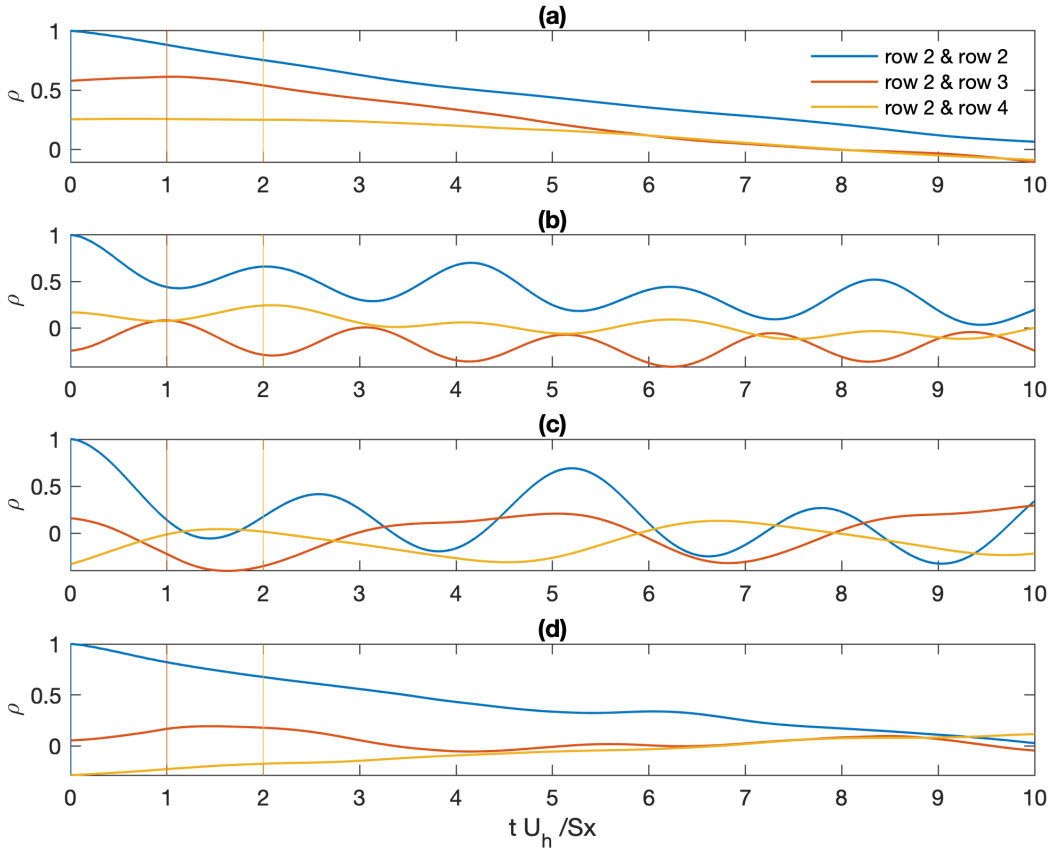


FIG. 25. Cross-correlation of turbine power signals for wind-only (a), 1.5Hz wave (b), 1.2Hz wave (c), and 1Hz wave (d) conditions. Vertical lines at $tU_h/S_x = 1$ & 2 indicate the convective flow time between row 2 and 3, and between row 2 and 4.

788 power shows distinct peaks at different frequencies, which can be related directly to wave
 789 frequencies, but also to spatial-temporal correlations in power fluctuations of turbines, due
 790 to the advection of turbulence and wave displacement. The wind advection time between two
 791 rows of turbines S_x/U_h , with the advection velocity estimated by the hub velocity, results in
 792 a phase lag between a turbine motion (and resulting power fluctuation) in one row, and the
 793 instance that a downwind turbine is exposed to a changed wake conditions (with resulting
 794 power fluctuation). The phase lag affects how much the power fluctuations are correlated, or
 795 anti-correlated. Similarly, the wave travel time between two rows of turbines S_x/v will result
 796 in a phase lag, which determines how the power fluctuations caused by turbine motion in one
 797 row will correlate or not with a downstream row. For the 1.5Hz wave condition, there is no

798 peak visible at the wave frequency (v/S_x) in the combined power spectrum, and the peak at
799 the wave frequency is also strongly reduced. It is expected that this is the result of the wave-
800 phase-lag partly anti-correlating the pitch motions. For example, the correlation coefficient
801 ρ of two sine functions with a frequency of 1.5Hz and phase shift of the wave travel time
802 $S_x/v \approx 0.9$ s, is $\rho \approx -0.6$, thus anti-correlating partly the pitching motion of two consecutive
803 turbine rows. Similarly, the phase shift of the wind-advection time is $S_x/U_h \approx 0.3$ s, resulting
804 in a correlation coefficient of $\rho \approx -1$. However, the effect of the wind-advection on the
805 correlation of power fluctuations from turbine motions is less straightforward, because it
806 relates a power fluctuation to a change in wind condition for the downstream turbine (for
807 example a deflected wake due to a yawed rotor movement), while the downstream turbine is
808 also making a motion which is triggered by the waves and phase-lagged with the wave travel
809 time. The combined power spectrum for a 1.2Hz wave still shows a distinct peak at the wave
810 frequency, though the wave travel time results in partly-anti-correlating. It is expected that
811 this is because for this wave condition, only the power signal of the turbine in row 2 shows
812 this peak distinctly. Thus not leading to significant canceling out between multiple rows.

813 At the frequency corresponding to the flow convection time between two rows U_h/S_x , and
814 the double of this frequency, all tested conditions (including the wind-only measurements)
815 show a broad, but less pronounced peak in the spectrum. This shows that even though the
816 aggregate is taken over a small number of turbines, and rows (i.e. three), a spatio-temporal
817 correlation in output power due to convection of turbulent structures results in a peak of
818 the power output. Similar observations were made for a fixed-bottom scaled wind farm
819 with twenty rows, subject to a turbulent boundary layer with long streamwise-meandering
820 turbulent structures [49]. The spatio-temporal sampling of the inflow by a wind farm was
821 described analytically, showing that for wind farms with more than three rows distinct peaks
822 can appear in the power spectrum if the inflow has large turbulent structures that remain
823 correlated over long distances as they travel through the wind farm [98, 99]. In the present
824 experiment, there is no space in the wind tunnel test-section to develop a boundary layer
825 with such long meandering structures. Given that we see these correlations in the aggregate
826 power over only three turbines, it is hypothesized that the motion of the turbines become
827 synchronized between different streamwise aligned turbines, due to wake interactions. This
828 can be the result of a turbine in row 2 making a sway motion, deflecting the wake, such
829 that a downstream turbine in the next row at a time S_x/U_h later notices a change in inflow

830 conditions, and moves in response. The broad peak at $fS_x/U_h = 1$ is also close to double
831 the wave frequencies, though no distinct peaks arise, except for the 1.5Hz wave condition,
832 for which the wave length is very close to the turbine spacing. For the 1.5Hz and 1.2Hz
833 wave there are two other distinct peaks in the range of $fS_x/U_h = 0.6 - 0.8$, which are also
834 seen in the individual spectrum of the turbine in row 2.

835 In figure 25, the measured cross-correlation of power signals between two turbines in the
836 middle of a row is shown as a function of time-delay between the signals. For the no-wave
837 condition, it is noticed that the auto correlation of the power signal stays correlated over a
838 very long time. This trend is especially noticeable when compared to results for fixed bottom
839 turbines subject to a turbulent boundary layer [95], which show distinct peaks at the turbine
840 spacing convective-time scale, but quickly become decorrelated over a time of $tU_h/Sx > 3$.
841 This indicates slow variations in power output, which may be a result of the slow sway
842 motions of the upstream turbine. Similarly, the cross-correlations with downstream turbines
843 remain correlated over a long time. A maximum cross-correlation is reached at a convective
844 flow-time corresponding to increments in turbine spacing, highlighting how slow turbine
845 motions can correlate the power outputs of downstream turbines via convected wakes. These
846 findings are in agreement with Fu et al. [39] who found an increased auto correlation of
847 the power signal for oscillating rotors. For the no-wave conditions, the maximum cross-
848 correlation in power output between row 2 and row 3 is around 0.55, which is similar in
849 magnitude as seen for fixed bottom turbine by Bossuyt et al. [95]. However, in this case the
850 high correlation is expected to be related to the effect of wake variations from slow turbine
851 motions (e.g. sway), instead of large turbulent structures, given that these are not present in
852 the inflow in this experiment. For the 1.5Hz and 1.2Hz wave conditions, the auto-correlation
853 of the power in row 2 shows a strong oscillation at the wave frequency due to the periodic
854 turbine motion. For the 1Hz wave, the oscillatory behavior has disappeared, highlighting the
855 slower and likely more variable motion over time. Interestingly, the cross-correlations with
856 downstream turbines are reduced in magnitude for these long period waves (< 0.25). As
857 discussed above, because of the phase-lag between motions in different rows, and due to the
858 wave velocity, the correlation from turbine motion is reduced for the conditions studied here.
859 For the no-wave condition, this is not the case, because the turbine motions are wind-driven
860 as wakes travel downstream affecting other turbines, synchronizing the motion frequency
861 with the convective flow frequency. For a wave condition of 1.5Hz, the instantaneous power

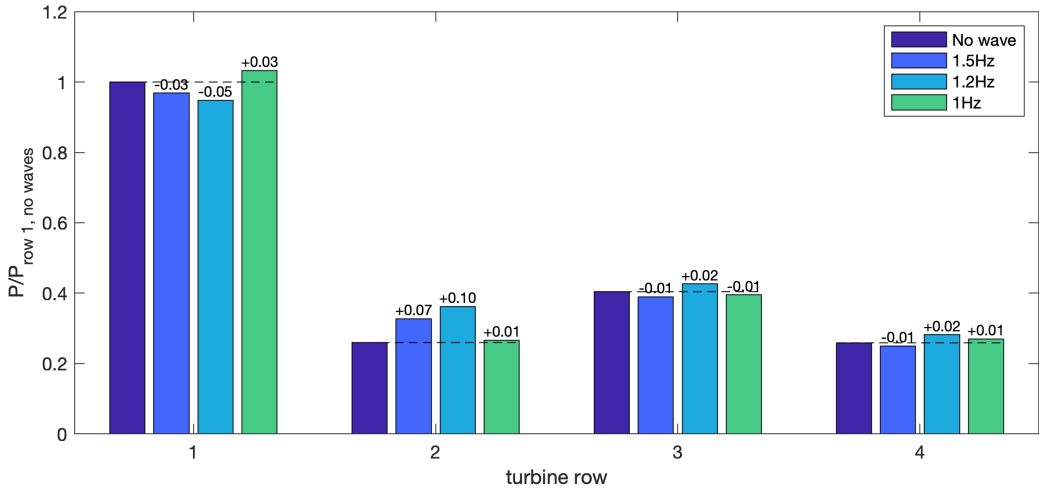


FIG. 26. Effect of wave conditions on power output of the middle turbine in each row. All measured power values are normalised by the power in the first row for the wind only condition. The normalized absolute power increase of each turbine compared to the wind-only condition is indicated above each bar.

862 of a turbine in row 2 and row 3 show a slight anti-correlation. This is a result of the wave
 863 having a wavelength equal to $0.7S_x$, anti-correlating the motion of the turbines slightly. For
 864 a wave of 1.2Hz, the wavelength measures $1.1S_x$, and is thus close to the turbine spacing,
 865 which explains the instantaneous correlation between row 2 and 3, and anti-correlation
 866 between row 2 and 4. Anti-correlations in turbine motion and resulting power output can
 867 result in reduced power fluctuations in the combined power output at certain frequencies.
 868 For example, in figure 24, the power spectrum of the 1Hz wave conditions is smaller than
 869 that of the no-wave condition in the 0.5-1Hz range, indicating an anti-correlation of turbine
 870 motions.

871 Figure 26 shows the mean power of the middle turbine in each row, normalized by the
 872 power of the middle turbine in the first row , for the wind-only condition ($P_i/P_{1,\text{no wind}}$). It
 873 can be seen that for the 1.5Hz and 1.2Hz wave condition the power in the first row reduced
 874 due to the increased misalignment. However, in the second row, the power increases more.
 875 This shows that the motion of the turbines studied in this paper can enhance wake recovery,
 876 especially in situations where the wake recovery is slow (e.g. the wake of the first row of
 877 turbines is subject to less background turbulence resulting in a smaller wake recovery rate).
 878 For the power of the turbine in the third row, the effect less pronounced. Compared to the

879 wind only condition, the total farm power increases with 0.7% when subject to 1.5Hz waves,
880 5% for 1.2Hz waves, and 2.1% for 1Hz waves.

881 VII. CONCLUSIONS

882 A floating wind farm experiment is scaled for measurements in the Portland State University
883 wind tunnel. A design approach that deviates from geometric similarity is introduced to
884 enable scaled floating turbine models with a realistic dynamic response even though Froude
885 scaling is unachievable at the desired scale ratio (1:400). The method is analogous to the
886 use of different low Reynolds number airfoil blade profiles and proportionally much larger
887 chord lengths for scaled wind tunnel tests of turbine rotors in order to reproduce realistic
888 dimensionless parameters for wake development (e.g. TSR , C_T , and C_P). Four scaling
889 ratios comparing the relative importance of wind and wave loads to the turbine inertia are
890 studied. These ratios highlight how the floater design can be adjusted to match the de-
891 sired dimensionless natural frequency for pitch and heave motions. Using this approach, a
892 scaled model floating turbine is designed, matching the dimensionless ratios of the target
893 turbine with a rotor diameter of 60m, and based on the OC5 DeepCWind floating platform.
894 Based on measurements of the free-decay response of tilt, and heave, it is confirmed that
895 the scaled natural frequencies are within the typical range for full-scale floating turbines.
896 The four dimensionless ratios provide insights into how the floating model platform can be
897 further adjusted and designed to scale to even larger rotor sizes.

898 The power and six-degrees of motion of a single turbine are characterized in a wind tunnel
899 test with different wind and wave conditions. Depending on the wave frequency, distinctly
900 different turbine motions are measured. Based on the wind-only test, it is concluded that the
901 platform pitch motion amplitude is within typical values for full-scale turbines (e.g. sway,
902 heave and surge motions on the order of or smaller than 0.05D, roll and yaw fluctuations
903 smaller than $\pm 0.5^\circ$, and pitch fluctuations of $\pm 2^\circ$ for wind-only conditions). The spectra of
904 the measured pitch motion trajectories show a strong signature of the wave frequency and
905 its harmonics and sub-harmonics (e.g., double and half the wave frequency), depending on
906 the motion and flow conditions. The Strouhal number of the wave frequency ranges around
907 $St = 0.05$ to $St = 0.08$, but motions with smaller amplitudes at higher harmonics up to
908 $St = 0.5$ are also triggered. The measured power coefficient for a wind speed of $U_h = 2.2\text{m/s}$

909 and $U_h = 4.3\text{m/s}$ shows only little Reynolds number sensitivity for the wind speed range of
910 interest (i.e. a variation in power coefficient of $C_p = 0.24$ to $C_p = 0.25$). The power spectral
911 density of the turbine power output shows a distinct peak at the wave frequency mostly
912 for the 1.5Hz wave condition, which triggers a strong pitching motion. For the 1.2Hz wave
913 condition a smaller peak at the wave frequency is seen, corresponding to a smaller pitch
914 motion at this frequency.

915 Wind tunnel measurements are then performed for a scaled wind farm with twelve floating
916 turbines (4 rows and 3 columns), for high wind conditions (corresponding to $U_h = 25\text{m/s}$ in
917 full-scale) and for three conditions with long-period ocean swell waves, and one wind-only
918 case. The power of the middle turbine in each row is measured, as well as the motion and
919 wake of the middle turbine in row 3, for the four different wave conditions. The turbine
920 motions show slowly varying sway variations for all wave conditions. Tests are performed
921 for wave frequencies close to, and below the natural frequency of the floating turbine model,
922 resulting in very distinct motion patterns. PIV measurements show clear differences in
923 wake recovery due to the periodic motions of the rotors. The 1.2Hz wave condition triggers
924 strong synchronized yaw and pitch motion, and results in increased wake recovery, but
925 also higher turbulence in the wake, which may affect unsteady loading of a downstream
926 rotor. By conditionally averaging the wake measurements with respect to wave-phase at the
927 measurement plane, a clear synchronization between wave induced rotor misalignment and
928 wake deflection is confirmed for all three conditions with long-period ocean wave conditions.
929 The power spectral density of scaled floating turbines in row 1 to row 4 shows distinct peaks
930 due to the induced rotor motions. Changes in the spectrum between different rows indicate
931 differences in motion due to different mean wind conditions, and differences in velocity
932 fluctuations due to the superposition of turbine wakes. The spectrum of the aggregate
933 power of rows 2, 3 and 4 shows a distinct peak at the wave frequency and half the wave
934 frequency for the 1.2Hz wave condition, which is characterized by strong yaw and pitch
935 motions. For the 1.5Hz wave condition, the peak at the wave frequency is still present but
936 strongly reduced, which could be a result of the phase shift between the pitching motion of
937 different rows, resulting from the wave phase velocity (e.g. S_x/v is equal to 0.6 times the
938 wave frequency of 1.5Hz, which is close to an anti correlation). It is expected that for the
939 1.2Hz wave condition the peak at the wave frequency is not canceled out, because the power
940 fluctuation at this frequency was mostly present for the turbine in the second row, and less

941 so for the others, thus not resulting in a canceling out of power fluctuations over multiple
942 rows. The cross-correlation of power outputs confirms a lower maximum cross-correlation
943 of power signals when the turbines are subject to the tested long-period waves, as compared
944 to the wind-only scenario. Compared to the correlations in power output of fixed bottom
945 turbines, which is mostly governed by turbulent spectra of the inflow [100], the power signals
946 can remain correlated over much longer times in the absence of long period swell waves, due
947 to slow variations in turbine position (mostly due to sway motions).

948 It is concluded that wind and water tunnel experiments of scaled floating wind farms
949 are possible when geometric scaling of the floaters is relaxed such that the dynamics can
950 be correctly matched (i.e. changes to the turbine platform design allow for relaxing Froude
951 scaling such that the Reynolds number can be kept large enough). These first experiments
952 with appropriately scaled model floating wind turbines confirm distinct impacts of turbine
953 motion on wake recovery and meandering, and highlight the intricate interactions of wave
954 topology, wake meandering and wind farm power production.

955 **Acknowledgements**

956 J.B. received funding from the Belgian American Education Foundation. DG and CM are
957 supported by NSF (grant # CMMI 2034111). OF, ZS, JB and RBC are supported by NSF
958 (grant # NSF-CMMI-2034160, NSF-CBET-2227263, and NSF-CBET-2037582).

959 **Appendix A: Particle Image Velocimetry setup**

960 Stereoscopic particle image velocimetry (S-PIV) is used to measure two-dimensional-
961 three-component (2-D-3C) velocity fields perpendicular to the main flow direction. The
962 S-PIV set-up consists of two 4M pixel CCD cameras and a Litron Nano double pulsed
963 Nd:YAG (532 nm, 1200 mJ, 4 ns duration) laser. The camera lenses have a focal length of
964 50mm. The cameras are oriented at an angle of 40 degrees with the measurement plane,
965 such that they have optical access between two rows of floating turbines, to a cross-plane at
966 a downstream distance of $x/D = 3$ from the center turbine in the third row. The thickness
967 of the laser sheet is approximately 4 mm. The uncertainty on the measured velocities is
968 estimated with Davis 10 software using the correlation statistics approach by Wieneke [101].
969 The estimated uncertainty over all planes is 0.01 m/s or smaller for all velocity components,
970 which corresponds to 0.2% of the freestream velocity during the tests ($U_0 = 4.1$ m/s).
971 The cameras are set up on one side of the wind tunnel. A Scheimpflug adapter is used
972 to correct the camera focus to the measurement plane. Neutrally buoyant fluid particles
973 of diethylhexyl sebacate are aerosolized by a seeding generator with a constant density
974 throughout the experiment. For each case, 5000 independent snapshot-pairs are recorded
975 at a frequency of 3.75Hz. Davis 10 software is used to apply a multipass Fourier transform-
976 based cross-correlation algorithm and apply a universal outlier detection method to filter
977 out any bad vectors. A multiple-pass reducing size interrogation window of 64×64 pixels
978 and 32×32 pixels, with a 50% overlap is used to process the data. The resulting vector
979 resolution is 2.2mm. Statistical averaging is performed by averaging over all S-PIV data
980 snapshots. During the PIV measurements, the fluorescence dye helped reduce reflections,
981 and made it possible to identify the water surface following the same approach explained in
982 section III A.

983 For tests with a single turbine, 2D-2C PIV is used to measure velocity fields in a stream-
984 wise aligned plane. The PIV setup consists of a single 4 megapixel CCD camera and the
985 same Litron Nano double pulsed Nd:YAG (532 nm, 1200 mJ, 4 ns duration) laser. The
986 camera lens has a focal length of 50 mm. For each measurement 500 independent image-
987 pairs are recorded at a frequency of 4 Hz, resulting in an estimated standard error of mean
988 velocity smaller than 0.5%. The uncertainty in Davis 10 is estimated as 0.4% of the free-
989 stream velocity for the horizontal velocity, and 0.25% for the vertical velocity component.

990 PIV processing is done in the same way as for the S-PIV measurements. The PIV window
991 covers an area of $0.2 \text{ m} \times 0.2 \text{ m}$, resulting in a vector resolution of 1.9mm.

992 **Appendix B: Hydrodynamic response sensitivity to floater dimensions**

993 The dependence of the tilt natural frequency to floater dimensions is verified by measuring
994 the response of several different floater designs. These measurement results are shown in
995 table VI, and are performed with an MPU6050 gyro and accelerometer connected to an
996 Arduino Due. The tests are done outside of the wind tunnel, with zero wind speed. The
997 weight of the rotor is represented by a simple porous disk. These tests are only used to make
998 a first evaluation of the required floater dimensions.

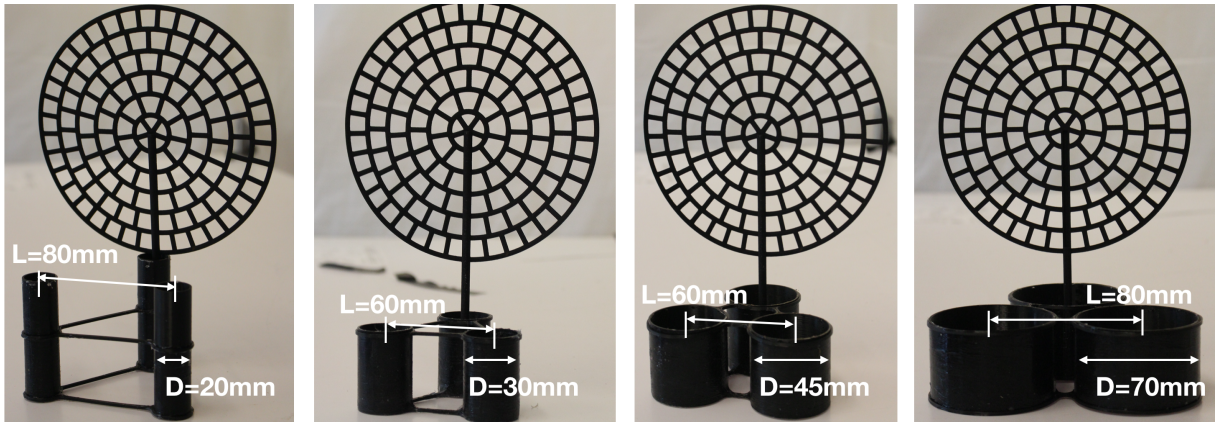


FIG. 27. Dummy floater designs to explore sensitivity of pitch response to floater dimensions and ballast.

999 [1] U.S. Department of the Interior, Biden-harris administration announces winners of
1000 California offshore wind energy auction, 2022. URL: <https://doi.gov/pressreleases/biden-harris-administration-announces-winners-california-offshore-wind-energy-auction>.

1001 [2] Offshore Wind Ireland, Floating wind in Scotland, 2022. URL: <https://www.offshorewindscotland.org.uk/the-offshore-wind-market-in-scotland/floating-wind-in-scotland/>.

Floater diameter [mm]	Floater spacing [mm]	Total mass [g]	Natural frequency for pitch [Hz]
20	80	53	0.9
30	60	55	1.1
30	60	77	1
45	60	46	2
45	60	158	1.85
70	80	105	2.4
70	80	325	2

TABLE VI. Overview of measured natural frequency of tilt for different dummy floater designs.

1005 [3] Reuters, Portugal ups debut offshore wind auction target to 10 GW,
 1006 2022. URL: [https://www.reuters.com/business/sustainable-business/](https://www.reuters.com/business/sustainable-business/portugal-ups-debut-offshore-wind-auction-target-10-gw-2022-09-21/)
 1007 [portugal-ups-debut-offshore-wind-auction-target-10-gw-2022-09-21/](https://www.reuters.com/business/sustainable-business/portugal-ups-debut-offshore-wind-auction-target-10-gw-2022-09-21/).

1008 [4] U.S. Department of Energy, Floating offshore wind shot, 2022. URL: <https://www.energy.gov/eere/wind/floating-offshore-wind-shot>.

1009 [5] A. J. Goupee, B. J. Koo, R. W. Kimball, K. F. Lambrakos, H. J. Dagher, Experimental
 1010 comparison of three floating wind turbine concepts, *Journal of Offshore Mechanics and Arctic*
 1011 *Engineering* 136 (2014).

1012 [6] A. R. Henderson, D. Witcher, C. A. Morgan, Floating support structures enabling new
 1013 markets for offshore wind energy, in: *Proceedings of the European Wind Energy Conference*
 1014 (EWEC), Marseille, France, volume 1619, 2009.

1015 [7] S. Butterfield, W. Musial, J. Jonkman, P. Sclavounos, Engineering challenges for floating
 1016 offshore wind turbines, *Technical Report, National Renewable Energy Lab.(NREL)*, Golden,
 1017 CO (United States), 2007.

1018 [8] A. Cordle, J. Jonkman, State of the art in floating wind turbine design tools, in: *The*
 1019 *twenty-first international offshore and polar engineering conference, OnePetro*, 2011.

1020 [9] S. Chakrabarti, Physical model testing of floating offshore structures, in: *Dynamic position-*
 1021 *ing conference*, volume 1, 1998, pp. 1–33.

1022 [10] P. Chen, J. Chen, Z. Hu, Review of experimental-numerical methodologies and challenges
 1023 for floating offshore wind turbines, *Journal of Marine Science and Application* 19 (2020)

1025 339–361.

1026 [11] M. F. Howland, J. Bossuyt, L. A. Martínez-Tossas, J. Meyers, C. Meneveau, Wake structure
1027 in actuator disk models of wind turbines in yaw under uniform inflow conditions, *Journal of*
1028 *Renewable and Sustainable Energy* 8 (2016) 043301.

1029 [12] C. Cossu, Evaluation of tilt control for wind-turbine arrays in the atmospheric boundary
1030 layer, *Wind Energy Science* 6 (2021) 663–675.

1031 [13] J. Bossuyt, R. Scott, N. Ali, R. B. Cal, Quantification of wake shape modulation and
1032 deflection for tilt and yaw misaligned wind turbines, *Journal of Fluid Mechanics* 917 (2021)
1033 A3.

1034 [14] C. R. Shapiro, D. F. Gayme, C. Meneveau, Modelling yawed wind turbine wakes: a lifting
1035 line approach, *Journal of Fluid Mechanics* 841 (2018) R1.

1036 [15] C. R. Shapiro, D. F. Gayme, C. Meneveau, Generation and decay of counter-rotating vortices
1037 downstream of yawed wind turbines in the atmospheric boundary layer, *Journal of Fluid*
1038 *Mechanics* 903 (2020) R2.

1039 [16] G. Narasimhan, D. F. Gayme, C. Meneveau, Effects of wind veer on a yawed wind turbine
1040 wake in atmospheric boundary layer flow, *Physical Review Fluids* 7 (2022) 114609.

1041 [17] M. Bastankhah, C. R. Shapiro, S. Shamsoddin, D. F. Gayme, C. Meneveau, A vortex sheet
1042 based analytical model of the curled wake behind yawed wind turbines, *Journal of Fluid*
1043 *Mechanics* 933 (2022) A2.

1044 [18] C. R. Shapiro, G. M. Starke, C. Meneveau, D. F. Gayme, A wake modeling paradigm for
1045 wind farm design and control, *Energies* 12 (2019) 2956.

1046 [19] D. Matha, M. Schlipf, A. Cordle, R. Pereira, J. Jonkman, Challenges in simulation of aero-
1047 dynamics, hydrodynamics, and mooring-line dynamics of floating offshore wind turbines,
1048 Technical Report, National Renewable Energy Lab.(NREL), Golden, CO (United States),
1049 2011.

1050 [20] S. Rockel, E. Camp, J. Schmidt, J. Peinke, R. B. Cal, M. Hölling, Experimental study on
1051 influence of pitch motion on the wake of a floating wind turbine model, *Energies* 7 (2014)
1052 1954–1985.

1053 [21] H. Kadum, S. Rockel, M. Hölling, J. Peinke, R. B. Cal, Wind turbine wake intermittency
1054 dependence on turbulence intensity and pitch motion, *Journal of Renewable and Sustainable*
1055 *Energy* 11 (2019).

1056 [22] R. Scott, J. Bossuyt, R. B. Cal, Characterizing tilt effects on wind plants, *Journal of*
1057 *Renewable and Sustainable Energy* 12 (2020).

1058 [23] H. Kadum, S. Rockel, B. Viggiano, T. Dib, M. Hölling, L. Chevillard, R. B. Cal, Assessing
1059 intermittency characteristics via cumulant analysis of floating wind turbines wakes, *Journal*
1060 *of Renewable and Sustainable Energy* 13 (2021).

1061 [24] R. Scott, L. Martínez-Tossas, J. Bossuyt, N. Hamilton, R. B. Cal, Evolution of eddy viscosity
1062 in the wake of a wind turbine, *Wind Energy Science Discussions* 2022 (2022) 1–22.

1063 [25] T. Messmer, M. Hölling, J. Peinke, Enhanced recovery and non-linear dynamics in the wake
1064 of a model floating offshore wind turbine submitted to side-to-side and fore-aft motion, *arXiv*
1065 preprint arXiv:2305.12247 (2023).

1066 [26] G. M. Starke, C. Meneveau, J. King, D. F. Gayme, Yaw-augmented control for wind farm
1067 power tracking, in: 2023 American Control Conference (ACC), IEEE, 2023, pp. 184–191.

1068 [27] T. Sebastian, M. Lackner, Characterization of the unsteady aerodynamics of offshore floating
1069 wind turbines, *Wind Energy* 16 (2013) 339–352.

1070 [28] R. Farrugia, T. Sant, D. Micallef, A study on the aerodynamics of a floating wind turbine
1071 rotor, *Renewable energy* 86 (2016) 770–784.

1072 [29] T. T. Tran, D. H. Kim, The aerodynamic interference effects of a floating offshore wind
1073 turbine experiencing platform pitching and yawing motions, *Journal of Mechanical Science*
1074 and Technology

1075 [30] T. T. Tran, D.-H. Kim, A cfd study into the influence of unsteady aerodynamic interference
1076 on wind turbine surge motion, *Renewable Energy* 90 (2016) 204–228.

1077 [31] H. Lee, D.-J. Lee, Effects of platform motions on aerodynamic performance and unsteady
1078 wake evolution of a floating offshore wind turbine, *Renewable Energy* 143 (2019) 9–23.

1079 [32] G. Chen, X.-F. Liang, X.-B. Li, Modelling of wake dynamics and instabilities of a floating
1080 horizontal-axis wind turbine under surge motion, *Energy* 239 (2022) 122110.

1081 [33] V. G. Kleine, L. Franceschini, B. S. Carmo, A. Hanifi, D. S. Henningson, The stability of
1082 wakes of floating wind turbines, *Physics of Fluids* 34 (2022) 074106.

1083 [34] Z. Li, G. Dong, X. Yang, Onset of wake meandering for a floating offshore wind turbine
1084 under side-to-side motion, *Journal of Fluid Mechanics* 934 (2022) A29.

1085 [35] N. Ramos-García, S. Kontos, A. Pegalajar-Jurado, S. González Horcas, H. Bredmose, Inves-
1086 tigation of the floating iea wind 15 mw rwt using vortex methods part i: Flow regimes and

1087 wake recovery, *Wind Energy* 25 (2022) 468–504.

1088 [36] R. Farrugia, T. Sant, D. Micallef, Investigating the aerodynamic performance of a model
1089 offshore floating wind turbine, *Renewable Energy* 70 (2014) 24–30.

1090 [37] T. Sant, D. Bonnici, R. Farrugia, D. Micallef, Measurements and modelling of the power
1091 performance of a model floating wind turbine under controlled conditions, *Wind Energy* 18
1092 (2015) 811–834.

1093 [38] I. Bayati, M. Belloli, L. Bernini, A. Zasso, Wind tunnel wake measurements of floating
1094 offshore wind turbines, *Energy Procedia* 137 (2017) 214–222.

1095 [39] S. Fu, Y. Jin, Y. Zheng, L. P. Chamorro, Wake and power fluctuations of a model wind
1096 turbine subjected to pitch and roll oscillations, *Applied Energy* 253 (2019) 113605.

1097 [40] B. Schliffke, S. Aubrun, B. Conan, Wind tunnel study of a “floating” wind turbine’s wake
1098 in an atmospheric boundary layer with imposed characteristic surge motion, in: *Journal of
1099 Physics: Conference Series*, volume 1618, IOP Publishing, 2020, p. 062015.

1100 [41] K. M. Kopperstad, R. Kumar, K. Shoele, Aerodynamic characterization of barge and spar
1101 type floating offshore wind turbines at different sea states, *Wind Energy* 23 (2020) 2087–2112.

1102 [42] A. Fontanella, I. Bayati, R. Mikkelsen, M. Belloli, A. Zasso, Unaflow: a holistic wind tunnel
1103 experiment about the aerodynamic response of floating wind turbines under imposed surge
1104 motion, *Wind Energy Science* 6 (2021) 1169–1190.

1105 [43] N. Belvasi, B. Conan, B. Schliffke, L. Perret, C. Desmond, J. Murphy, S. Aubrun, Far-wake
1106 meandering of a wind turbine model with imposed motions: An experimental s-piv analysis,
1107 *Energies* 15 (2022) 7757.

1108 [44] A. Fontanella, A. Zasso, M. Belloli, Wind tunnel investigation of the wake-flow response
1109 for a floating turbine subjected to surge motion, in: *Journal of Physics: Conference Series*,
1110 volume 2265, IOP Publishing, 2022, p. 042023.

1111 [45] H. Meng, H. Su, T. Qu, L. Lei, Wind tunnel study on the wake characteristics of a wind
1112 turbine model subjected to surge and sway motions, *Journal of Renewable and Sustainable
1113 Energy* 14 (2022) 013307.

1114 [46] R. B. Cal, J. Lebrón, L. Castillo, H. S. Kang, C. Meneveau, Experimental study of the
1115 horizontally averaged flow structure in a model wind-turbine array boundary layer, *Journal
1116 of renewable and sustainable energy* 2 (2010) 013106.

1117 [47] M. Calaf, C. Meneveau, J. Meyers, Large eddy simulation study of fully developed wind-
1118 turbine array boundary layers, *Physics of fluids* 22 (2010) 015110.

1119 [48] N. Hamilton, H. Suk Kang, C. Meneveau, R. Bayoán Cal, Statistical analysis of kinetic
1120 energy entrainment in a model wind turbine array boundary layer, *Journal of renewable and*
1121 *sustainable energy* 4 (2012) 063105.

1122 [49] J. Bossuyt, C. Meneveau, J. Meyers, Effect of layout on asymptotic boundary layer regime
1123 in deep wind farms, *Physical Review Fluids* 3 (2018) 124603.

1124 [50] J. Bossuyt, M. Howland, C. Meneveau, J. Meyers, Measuring power output intermittency
1125 and unsteady loading in a micro wind farm model, in: 34th Wind Energy Symposium, 2016,
1126 p. 1992.

1127 [51] E. H. Camp, R. B. Cal, Low-dimensional representations and anisotropy of model rotor
1128 versus porous disk wind turbine arrays, *Physical Review Fluids* 4 (2019) 024610.

1129 [52] N. Hamilton, B. Viggiano, M. Calaf, M. Tutkun, R. B. Cal, A generalized framework for
1130 reduced-order modeling of a wind turbine wake, *Wind Energy* 21 (2018) 373–390.

1131 [53] G. Cortina, M. Calaf, R. B. Cal, Distribution of mean kinetic energy around an isolated
1132 wind turbine and a characteristic wind turbine of a very large wind farm, *Physical Review*
1133 *Fluids* 1 (2016) 074402.

1134 [54] E. H. Camp, R. B. Cal, Mean kinetic energy transport and event classification in a model
1135 wind turbine array versus an array of porous disks: Energy budget and octant analysis,
1136 *Physical Review Fluids* 1 (2016) 044404.

1137 [55] Z. Sadek, R. Scott, N. Hamilton, R. B. Cal, A three-dimensional, analytical wind turbine
1138 wake model: Flow acceleration, empirical correlations, and continuity, *Renewable Energy*
1139 209 (2023) 298–309.

1140 [56] S. E. Smith, K. N. Travis, H. Djeridi, M. Obligado, R. B. Cal, Dynamic effects of inertial
1141 particles on the wake recovery of a model wind turbine, *Renewable Energy* 164 (2021)
1142 346–361.

1143 [57] R. Scott, B. Viggiano, T. Dib, N. Ali, M. Hölling, J. Peinke, R. B. Cal, Wind turbine partial
1144 wake merging description and quantification, *Wind Energy* 23 (2020) 1610–1618.

1145 [58] N. Ali, R. B. Cal, Data-driven modeling of the wake behind a wind turbine array, *Journal*
1146 *of Renewable and Sustainable Energy* 12 (2020).

1147 [59] D. Yang, C. Meneveau, L. Shen, Large-eddy simulation of offshore wind farm, *Physics of*
1148 *Fluids* 26 (2014) 025101.

1149 [60] O. Ferčák, J. Bossuyt, N. Ali, R. B. Cal, Decoupling wind–wave–wake interactions in a
1150 fixed-bottom offshore wind turbine, *Applied Energy* 309 (2022) 118358.

1151 [61] H. Yang, M. Ge, M. Abkar, X. I. Yang, Large-eddy simulation study of wind turbine array
1152 above swell sea, *Energy* 256 (2022) 124674.

1153 [62] T. Hegberg, G. Corten, P. Schaak, Turbine interaction in large offshore wind farms. wind
1154 tunnel measurements (2004).

1155 [63] L. P. Chamorro, R. E. Arndt, F. Sotiropoulos, Reynolds number dependence of turbulence
1156 statistics in the wake of wind turbines, *Wind Energy* 15 (2012) 733–742.

1157 [64] M. Bastankhah, F. Porté-Agel, A new miniature wind turbine for wind tunnel experiments.
1158 part i: Design and performance, *Energies* 10 (2017) 908.

1159 [65] S. A. Hughes, Physical models and laboratory techniques in coastal engineering, volume 7,
1160 World Scientific, 1993.

1161 [66] V. Heller, Scale effects in physical hydraulic engineering models, *Journal of Hydraulic*
1162 *Research* 49 (2011) 293–306.

1163 [67] J. Jonkman, S. Butterfield, W. Musial, G. Scott, Definition of a 5-MW reference wind turbine
1164 for offshore system development, Technical Report, National Renewable Energy Lab.(NREL),
1165 Golden, CO (United States), 2009.

1166 [68] G. Stewart, M. Muskulus, A review and comparison of floating offshore wind turbine model
1167 experiments, *Energy Procedia* 94 (2016) 227–231.

1168 [69] M. A. Miller, J. Kiefer, C. Westergaard, M. O. Hansen, M. Hultmark, Horizontal axis wind
1169 turbine testing at high reynolds numbers, *Physical Review Fluids* 4 (2019) 110504.

1170 [70] M. J. Fowler, R. W. Kimball, D. A. Thomas III, A. J. Goupee, Design and testing of scale
1171 model wind turbines for use in wind/wave basin model tests of floating offshore wind turbines,
1172 in: *International Conference on Offshore Mechanics and Arctic Engineering*, volume 55423,
1173 American Society of Mechanical Engineers, 2013, p. V008T09A004.

1174 [71] A. Otter, J. Murphy, V. Pakrashi, A. Robertson, C. Desmond, A review of modelling
1175 techniques for floating offshore wind turbines, *Wind Energy* 25 (2022) 831–857.

1176 [72] L. P. Chamorro, F. Porté-Agel, Turbulent flow inside and above a wind farm: a wind-tunnel
1177 study, *Energies* 4 (2011) 1916–1936.

1178 [73] W. Zhang, C. D. Markfort, F. Porté-Agel, Wind-turbine wakes in a convective boundary
1179 layer: A wind-tunnel study, *Boundary-layer meteorology* 146 (2013) 161–179.

1180 [74] H. C. Lim, I. P. Castro, R. P. Hoxey, Bluff bodies in deep turbulent boundary layers:
1181 Reynolds-number issues, *Journal of Fluid Mechanics* 571 (2007) 97–118.

1182 [75] A. N. Robertson, F. Wendt, J. M. Jonkman, W. Popko, H. Dagher, S. Gueydon, J. Qvist,
1183 F. Vittori, J. Azcona, E. Uzunoglu, et al., Oc5 project phase ii: validation of global loads of
1184 the deepcwind floating semisubmersible wind turbine, *Energy Procedia* 137 (2017) 38–57.

1185 [76] D. Marten, Qblade: a modern tool for the aeroelastic simulation of wind turbines (2020).

1186 [77] H. R. Martin, Development of a scale model wind turbine for testing of offshore floating
1187 wind turbine systems (2011).

1188 [78] M. P. Buckley, F. Veron, The turbulent airflow over wind generated surface waves, *European
1189 Journal of Mechanics-B/Fluids* 73 (2019) 132–143.

1190 [79] N. Machicoane, A. Aliseda, R. Volk, M. Bourgoin, A simplified and versatile calibration
1191 method for multi-camera optical systems in 3d particle imaging, *Review of Scientific Instruments* 90 (2019) 035112.

1192 [80] N. Hamilton, M. Melius, R. B. Cal, Wind turbine boundary layer arrays for cartesian and
1193 staggered configurations-part i, flow field and power measurements, *Wind Energy* 18 (2015)
1194 277–295.

1195 [81] A. S. Aseyev, R. B. Cal, Vortex identification in the wake of a model wind turbine array,
1196 *Journal of Turbulence* 17 (2016) 357–378.

1197 [82] N. Ali, N. Hamilton, D. DeLucia, R. Bayoán Cal, Assessing spacing impact on coherent
1198 features in a wind turbine array boundary layer, *Wind Energy Science* 3 (2018) 43–56.

1199 [83] Y. Odemark, J. H. Fransson, The stability and development of tip and root vortices behind
1200 a model wind turbine, *Experiments in fluids* 54 (2013) 1–16.

1201 [84] A. J. Coulling, A. J. Goupee, A. N. Robertson, J. M. Jonkman, H. J. Dagher, Validation
1202 of a fast semi-submersible floating wind turbine numerical model with deepcwind test data,
1203 *Journal of Renewable and Sustainable Energy* 5 (2013) 023116.

1204 [85] J. Azcona, F. Bouchotrouch, M. González, J. Garciadía, X. Munduate, F. Kelberlau, T. A.
1205 Nygaard, Aerodynamic thrust modelling in wave tank tests of offshore floating wind turbines
1206 using a ducted fan, in: *Journal of Physics: Conference Series*, volume 524, IOP Publishing,
1207 2014, p. 012089.

1209 [86] M. T. Hall, Hybrid modeling of floating wind turbines, The University of Maine, 2016.

1210 [87] A. N. Robertson, J. M. Jonkman, A. J. Goupee, A. J. Coulling, I. Prowell, J. Browning, M. D.
1211 Masciola, P. Molta, Summary of conclusions and recommendations drawn from the deep-
1212 cwind scaled floating offshore wind system test campaign, in: International Conference on
1213 Offshore Mechanics and Arctic Engineering, volume 55423, American Society of Mechanical
1214 Engineers, 2013, p. V008T09A053.

1215 [88] L. Li, Y. Gao, Z. Hu, Z. Yuan, S. Day, H. Li, Model test research of a semisubmersible floating
1216 wind turbine with an improved deficient thrust force correction approach, *Renewable energy*
1217 119 (2018) 95–105.

1218 [89] S. Gueydon, Aerodynamic damping on a semisubmersible floating foundation for wind tur-
1219 bines, *Energy Procedia* 94 (2016) 367–378.

1220 [90] E. E. Bachynski, M. Etemaddar, M. I. Kvitem, C. Luan, T. Moan, Dynamic analysis of
1221 floating wind turbines during pitch actuator fault, grid loss, and shutdown, *Energy Procedia*
1222 35 (2013) 210–222.

1223 [91] A. J. Goupee, M. J. Fowler, R. W. Kimball, J. Helder, E.-J. de Ridder, Additional wind/wave
1224 basin testing of the deepcwind semi-submersible with a performance-matched wind turbine,
1225 in: International Conference on Offshore Mechanics and Arctic Engineering, volume 45547,
1226 American Society of Mechanical Engineers, 2014, p. V09BT09A026.

1227 [92] J. Lighthill, *Waves in fluids*, Cambridge university press, 2001.

1228 [93] C. D. Markfort, W. Zhang, F. Porté-Agel, Analytical model for mean flow and fluxes of
1229 momentum and energy in very large wind farms, *Boundary-Layer Meteorology* 166 (2018)
1230 31–49.

1231 [94] N. G. Nygaard, Wakes in very large wind farms and the effect of neighbouring wind farms,
1232 in: *Journal of Physics: Conference Series*, volume 524, IOP Publishing, 2014, p. 012162.

1233 [95] J. Bossuyt, M. F. Howland, C. Meneveau, J. Meyers, Measurement of unsteady loading and
1234 power output variability in a micro wind farm model in a wind tunnel, *Experiments in Fluids*
1235 58 (2017) 1–17.

1236 [96] M. Hall, A. Goupee, Validation of a lumped-mass mooring line model with deepcwind
1237 semisubmersible model test data, *Ocean Engineering* 104 (2015) 590–603.

1238 [97] B. Skaare, F. G. Nielsen, T. D. Hanson, R. Yttervik, O. Havmøller, A. Rekdal, Analysis of
1239 measurements and simulations from the hywind demo floating wind turbine, *Wind Energy*

1240 18 (2015) 1105–1122.

1241 [98] I. Marusic, Evidence of very long meandering features in the logarithmic region of turbulent
1242 boundary layers, *Journal of Fluid Mechanics* 579 (2007) 1–28.

1243 [99] L. J. Lukassen, R. J. Stevens, C. Meneveau, M. Wilczek, Modeling space-time correlations
1244 of velocity fluctuations in wind farms, *Wind energy* 21 (2018) 474–487.

1245 [100] J. Bossuyt, C. Meneveau, J. Meyers, Wind farm power fluctuations and spatial sampling of
1246 turbulent boundary layers, *Journal of Fluid Mechanics* 823 (2017) 329–344.

1247 [101] B. Wieneke, Piv uncertainty quantification from correlation statistics, *Measurement Science
1248 and Technology* 26 (2015) 074002.